Ionic Liquids at Air/ Water Interface

Raquel Marisa Moreira Valente

Thesis to obtain the Master of Science Degree in

Chemical Engineering

Supervisors: Professor Doctor Eduardo Jorge Morilla Filipe

Doctor Philippe Fontaine

Examination Committee

Chairperson: Professor Doctor Benilde de Jesus Vieira Saramago

Supervisor: Professor Doctor Eduardo Jorge Morilla Filipe

Member of the Committee: Professor Doctor Isabel Maria Delgado Jana Marrucho Ferreira

November 2016

Ionic Liquids at Air/ Water Interface

Raquel Marisa Moreira Valente

Thesis to obtain the Master of Science Degree in

Chemical Engineering

Supervisors: Professor Doctor Eduardo Jorge Morilla Filipe (IST)

Doctor Philippe Fontaine (SOLEIL)

Examination Committee

Chairperson: Professor Doctor Benilde de Jesus Vieira Saramago

Supervisor: Professor Doctor Eduardo Jorge Morilla Filipe

Member of the Committee: Professor Doctor Isabel Maria Delgado Jana Marrucho Ferreira

November 2016

Acknowledgements

Abstract

Ionic Liquids (ILs) are a class of new solvents considered as environmental friendly for chemical processes. ILs consist solely of ions which asymmetric shape inhibits solidification near room temperature. In the last few years their popularity increased due to its unique properties, strongly dependent on cation and anion chosen, and therefore a large number of application have been proposed. Detailed knowledge of the ion organization at the interface of ILs can be very important and interesting to many processes.

In the present work, it is proposed to obtain a better understanding of the behaviour as well as the structure of $[C_n mim][NTf_2]$ (n=12, 14, 16, 18) ILs family at air/ pure water and air/ salt water interfaces through the Langmuir monolayer techniques. It is presented results obtained on Langmuir monolayers of ILs by (π-A) isotherms, Brewster Angle Microscopy, Grazing Incidence X-ray Diffraction (GIXD), Total Reflection X-ray fluorescence (TXRF) and X-ray Powder Diffraction (XRD).

Key Words

Ionic Liquids, $[C_{18}mim][NTf_2]$, Langmuir Monolayer, X-ray, GIXD, Interfaces

Resumo

Os Líquidos Iónicos (LIs) são uma classe de novos solventes considerados ecológicos para processos químicos. Os LIs consistem unicamente em iões que apresentam uma forma assimétrica que inibe a sua solidificação a uma temperatura próxima da temperatura ambiente. Nos últimos anos a sua popularidade aumentou devido às suas propriedades únicas, que dependem fortemente da combinação do catião e anião escolhidos, e, deste modo, um grande número de aplicações têm vindo a ser propostas. O conhecimento detalhado da organização iónica dos LIs em interfaces pode ser bastante importante e interessante para muitos processos.

No presente trabalho, propõe-se obter uma melhor compreensão do comportamento, bem como da estrutura dos LIs pertencentes à família $[C_n mim][NTf_2]$ (n=12, 14, 16, 18) nas interfaces ar/ água pura e ar/ água salgada através de técnicas da monocamada de Langmuir. São apresentados resultados obtidos da monocamada de Langmuir dos LIs através das curvas de isotérmicas (π-A), Microscopia no Ângulo de Brewster (BAM), Difracção de Raios-X com Ângulo de Incidência Rasante (GIXD), Fluorescência de Raios-X por Reflexão Total (TXRF) e Difracção de pó (XRD).

Palavras-chave

Líquidos Iónicos, $[C_{18}mim][NTf_2]$, Monocamada de Langmuir, Raio-X, GIXD, Interfaces

Contents

Index to Figure

Index to Tables

Acronyms

A – Area per molecule

A_0 – Equilibrium area per molecule

BAM – Brewster Angle Microscopy

ESP – Equilibrium spreading pressure

d – dimension of the plate (Langmuir Techniques); and Inter planar distance (BAM)

F – downward force on suspended plate (Langmuir Techniques)

GIXD – Grazing Incidence X-ray Diffraction

IL – Ionic Liquids

n – Positive integer (BAM)

n – Refractive index (BAM)

RTIL – Room temperature ionic liquids

t – time

T_m – Melting point

TXRF – Total Reflection X-ray Fluorescence

VOC – Volatile organic compounds

w – dimension of the plate (Langmuir Techniques)

XRD – X-ray Powder Diffraction

Greek Symbols

γ – Surface tension

θ – angle

π – Surface pressure

λ – wavelength

Isotherm Names

ISOT **N Y** – isotherm of the molecule [$C_n$mim] [NTf_2] at **air/ pure water interface** performed at a compression rate of **Y** after waiting **10 minutes** of solvent evaporation;

ISOT**S N Y** – isotherm of the molecule [$C_n$mim] [NTf_2] at **air/ salt water interface** performed at a compression rate of **Y** after waiting **10 minutes** of solvent evaporation;

ISOT **N Z** – isotherm of the molecule [$C_n$mim] [NTf_2] at **air/ pure water interface** performed at a compression rate of **20 cm^2 min^{-1} (0.0002 nm^2 sec^{-1} molecule^{-1})** after waiting **Z** of solvent evaporation;

ISOT**S N Z** – isotherm of the molecule [$C_n$mim] [NTf_2] at **air/ salt water interface** performed at a compression rate of **20 cm^2 min^{-1} (0.0002 nm^2 sec^{-1} molecule^{-1})** after waiting **Z** of solvent evaporation;

N: 12, 14, 16 or 18

Y: - **60**: 20 cm^2 min^{-1} (0.0002 nm^2 sec^{-1} molecule^{-1})
- **120**: 36 cm^2 min^{-1} (0.0004 nm^2 sec^{-1} molecule^{-1})
- **240**: 69 cm^2 min^{-1} (0.0008 nm^2 sec^{-1} molecule^{-1})

Z: - **N**: one night ($\approx$15 hours)
- **WE**: one weekend ($\approx$65hours)

Molecules

[C_{18}mim] [Cl] = 1-octadecyl-3-methylimidazolium chlorine

[C_{12}mim] [NTf_2] = 1-dodecyl-3-methylimidazolium bis(trifluoromethylsulfonyl)imide

[C_{14}mim] [NTf_2] = 1-tetradecyl-3-methylimidazolium bis(trifluoromethylsulfonyl)imide

[C_{16}mim] [NTf_2] = 1-hexadecyl-3-methylimidazolium bis(trifluoromethylsulfonyl)imide

[C_{18}mim] [NTf_2] = 1-octadecyl-3-methylimidazolium bis(trifluoromethylsulfonyl)imide

[C_{18}mim] [PF_6] = 1-octadecyl-3-methylimidazolium hexafluorophosphate

I. Introduction

Ionic liquids (ILs) are salts with melting point much lower than usual salts, $T_m \leq 100°C$, i.e., below the boiling point of water; some of them even melt below $0°C$ (Figure 1). Some authors also differentiate ILs from Room-Temperature Ionic Liquids (RTILs), which melt at temperatures below 25 °C. These ILs, in contrast with salt solution, consist entirely of cations and anions, without a presence of any solvent. Until one hundred years ago, it was never imagined that, at room temperature, ions could form a liquid unless diluted in a solvent. (Hayes, Warr, & Atkin, 2015; Wasserscheid & Welton, 2002) When comparing a typical IL with a typical inorganic salt, with single or few atom cations and anions (eg. NaCl, $ZnBr_2$ or $NaNO_3$), the clear difference between both is their chemical structure. ILs show an asymmetric shape, which results in a destabilization of the crystalline lattice, reducing the melting point and increasing the liquidus range of the IL. (Aldrich, 2005; Sloutskin et al., 2005)
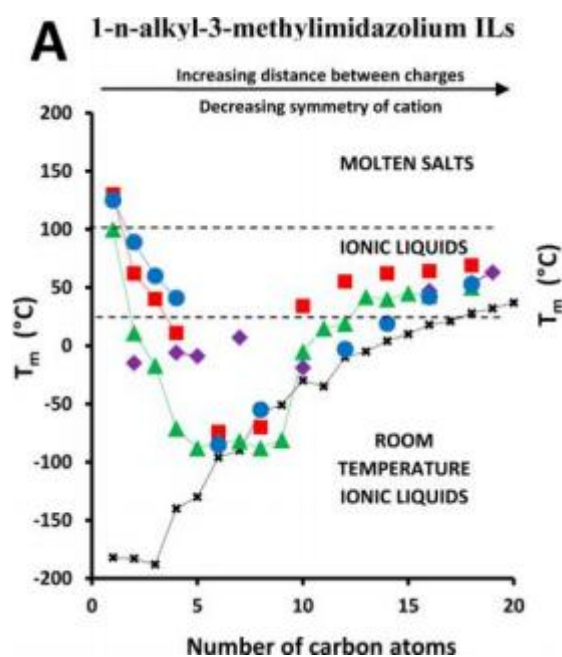
Figure 1 - Melting point (Tm) as a function of cation alkyl chain length (n) for salts systems with 1-n-alkyl-3-methylimidazolium cations. n-Alkane data (n = 1− 20, black x) are also shown for comparison. Dashed lines indicate the boundaries between molten salts (Tm > 100 °C), ILs (Tm ≤ 100 °C) and RTILs (Tm ≤ 25 °C). Each curve represents a different combination of the cation with the following anions: hexafluorophosphate ([PF₆]⁻, red■), tetrafluoroborate ([BF₄]⁻, green▲), bis(perfluoromethyl-sulfonyl)imide ([NTf₂]⁻, purple◆) and chloride ([Cl]⁻, blue●). (Hayes et al., 2015)

The popularity of ILs increased in last years, mainly because of two advantages over traditional solvents:

- They are considered as an environmental friendly alternative to the volatile organic compounds (VOCs) used as a solvent in industry. When compared to VOCs, ILs typically have very low volatility, due to their strong ionic (coulomb) interaction: their vapor pressures are extremely low and have to be obtained at very high temperatures, therefore information about their vapor pressures are scarce in the literature. (Tavares, Rodriguez, & Macedo, 2013) ILs have other advantageous properties, such as, nonflammable, high viscosity, thermal stability, ability to dissolve a wide range of compounds, controlled miscibility with organic solvents and a wide electrochemical window. Beyond that they can be frequently recycled (Tamam, Ocko, Reichert, & Deutsch, 2011; Tavares et al., 2013);
- The properties of ILs strongly depend on the cation and anion chosen. There are around one million possible combinations that can be made in order to obtain the desirable properties.

Indeed, all these unique properties are the reason of the increase of the number of publications concerning ILs in the last years (Figure 2) and therefore of the number of applications of ILs. ILs have been studied for different applications such as in medicine (Wu, Chen, Fan, Elsebaei, & Zhu, 2012); as a solvent in industry, both in chemical and enzymatic biocatalysis (Plechkova et al., 2008; Tavares et al., 2013; Welton, 1999); as an electrolyte (Kuboki, Okuyama, Ohsaki, & Takami, 2005; Lewandowski & Świderska-Mocek, 2009; Rogers & Seddon, 2003; Zhao, Hu, Li, Wang, & Chen, 2011), among other applications.
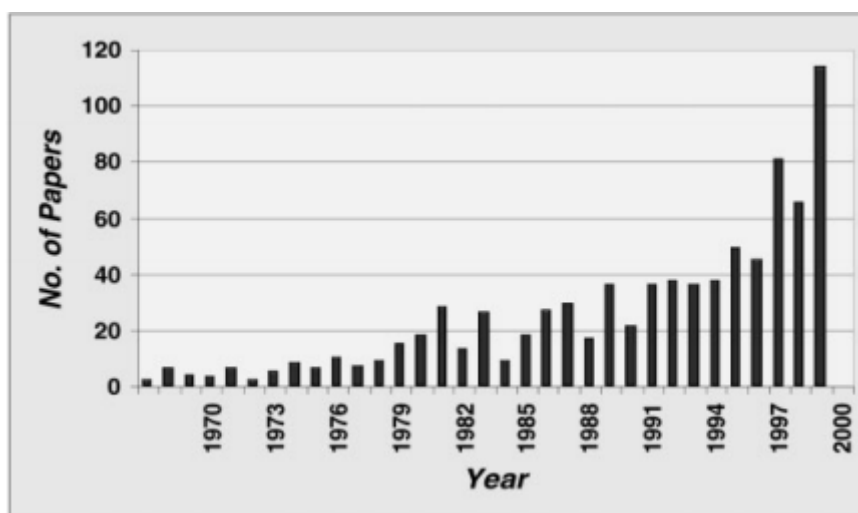
Figure 2 – The increase in publication concerning ILs as a function of time (determined using SciFinder). (Wasserscheid & Welton, 2002)

For potential application of processes at interfaces, ILs are often involved but poorly investigated from a fundamental point of view. The knowledge of the ion organization at interfaces and its interfacial properties can be very important and interesting. ILs with long alkyl chain are amphiphilic molecules, with a hydrophobic and a hydrophilic part, thereby it should be notice that they can show a similar behaviour to those shown by ionic surfactants forming structures as micelles. Thus, this type of ILs could also form Langmuir monolayers, a molecular thick layer of amphiphilic molecules, with the hydrophilic head groups down and the hydrophobic tail groups up, that can be studied through Langmuir techniques. Despite their great potential, this area is a largely unexplored field:

- Bai *et al.* (Bai, Li, & Zheng, 2010) reported synthesis of a gold nanoparticles in a two-phase liquid/ liquid system, using S-3-hexadecyl-1-(2- hydroxy-1-methylethyl) imidazolium bromide ([C_{16}hmim]Br) as a monolayer-stabilizer;
- Later, Jia *et al.* (Jia et al., 2012) prepared Gold nanochains at the air/ water interface, using 1-hexadecyl-3-methylimidazolium bromide (C_{16}mimBr) as a monolayer-stabilizer.
- Mukherjee *et al.* (Mukherjee, Mukherjee, Naskar, Ghosh, & Moulik, 2013) reported the study of solution and surface chemical behavior of two ILs triisobutyl(methyl)phosphonium tosylate ([$P_{1,4,4,4}$][tos]) and trihexyl(tetradecyl)phosphonium bis 2,4,4-(trimethylpentyl)phosphinate ([P_{66614}][(iC_8)$_2PO_2$]). Langmuir Monolayer formation is addressed;
- Tamam *et al.* (Tamam et al., 2011) reported the study of a Langmuir film of 1-butyl- 1-methylpyrrolidinium tris(pentafluoroethyl) trifluorophosphate ([BMPL][FAP]) on mercury;
- Recently, Filipe *et al.* (Filipe et al., 2016) reported the formation of Langmuir films of [C_{18}mim][NTf_2] at air/ water interface. Molecular dynamics simulation supported experimental results.

In the present project, it is proposed to study the behavior of six different ILs with one long chain and its structure at the air/ pure and air/ salt water interfaces. The cations that were chosen are imidazolium based ([$C_n$mim]+, n=12, 14, 16 and 18, Figure 3). It was chosen a family of ILs with a long chain that showed to give the insoluble character mandatory for an amphiphilic molecule. Moreover, the studies about its Langmuir monolayer are scarce even though imidazolium IL are one of the most considered IL for applications.

Regarding the anions, it was chosen three different (Figure 4): a smaller one ([Cl]⁻), another larger but with spherical shape ([PF_6]⁻) and finally a non-spherical one with internal mobility ([(CF_3SO_2)$_2$N =NTf_2]⁻ or [NTf_2]⁻). Those anions were chosen to study different types of combinations of ILs. To study this family with [Cl]⁻ and [PF_6]⁻, it was chosen to just perform the experiments only with [C_{18}mim]+.

The behaviour of those six ILs and their structure at the air/ pure and air/ salt water interfaces were studied at different length scales: macroscopic, by surface tension measurements during different compression/ decompression cycles; microscopic, by images obtained by Brewster Angle Microscopy (BAM); and nanometric and molecular, by X-Ray Experiments, Grazing Incidence X-ray Diffraction (GIXD), Total Reflection X-ray Fluorescence (TXRF) and X-ray Powder Diffraction (XRD).

(a)	(b)
	H_3C ⋯⋯⋯⋯⋯⋯⋯⋯⋯⋯⋯ CH_3 18
	(c)
	H_3C ⋯⋯⋯⋯⋯⋯⋯⋯⋯ CH_3 16
R^1—N—N⁺—CH_3	(d)
	H_3C ⋯⋯⋯⋯⋯⋯⋯ CH_3 14
	(e)
	H_3C ⋯⋯⋯⋯⋯ CH_3 12
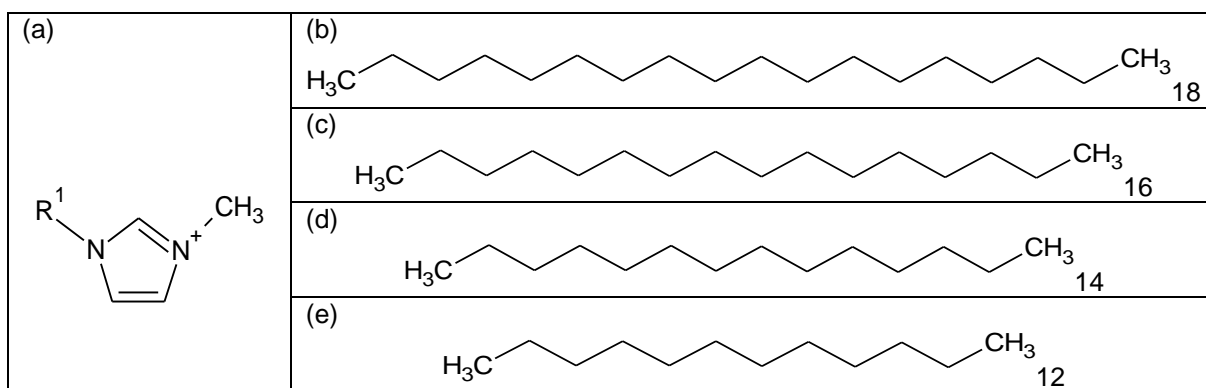
Figure 3 – Cations imidazolium based chosen for this project. In (a) Imidazolium group, the group R^1 can be replaced for (b), (c), (d) or (e), depending on the cation. The name of the cation is, when R^1 is replaced for, (b) 1-octadecyl-3-methylimidazolium ($[C_{18}mim]^+$) ; (c) 1-hexadecyl-3-methylimidazolium ($[C_{16}mim]^+$) ; (d) 1-tetradecyl-3-methylimidazolium ($[C_{14}mim]^+$) ; and (e) 1-dodecyl-3-methylimidazolium ($[C_{12}mim]^+$).

| (a) | (b) | (c) |
| Cl^- | PF_6^- | $[NTf_2]^-$ |
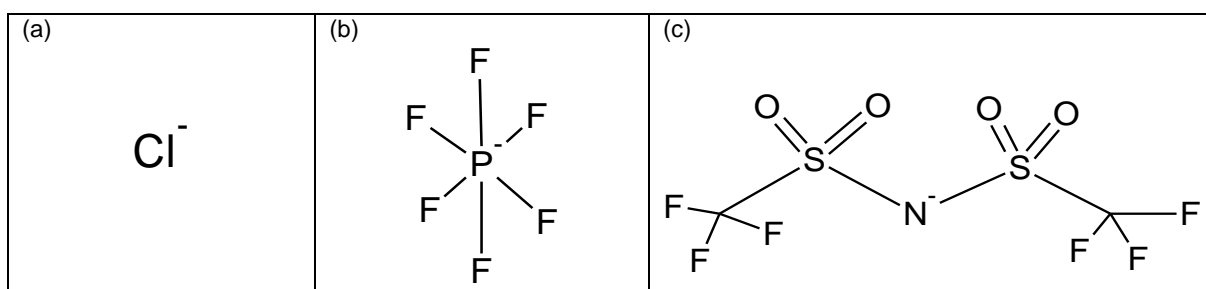
Figure 4 – Anions chosen for this project. In (a) chlorine ($[Cl]^-$) ; (b) hexafluorophosphate ($[PF_6]^-$); and (c) bis(trifluoromethylsulfonyl)imide ($[NTf_2]^-$).

II. Experimental Techniques

II.1. Langmuir technique

As said on Chapter I Introduction, a Langmuir monolayer is a molecular thick layer of amphiphilic molecules, with the hydrophilic head groups down, anchoring the molecule at the air/ aqueous solution interface and the hydrophobic tail groups up, preventing dissolution of the molecules (Figure 5).
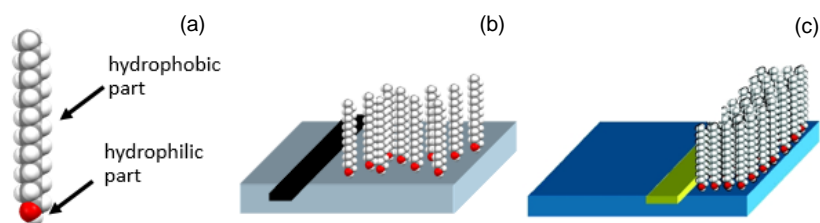
Figure 5 – Amphiphilic molecule (a) and Langmuir Monolayer at large surface densities (b) and at small surface densities (c).

To study Langmuir monolayers at the air/ aqueous solution interface, Langmuir troughs are used (Figure 6). This technique uses a shallow Teflon trough, previously cleaned and rinsed, filled to the border with an aqueous subphase. With a trough full, the spreading can be made. The subphases used in this work were pure water and water with NaCl (salt water).
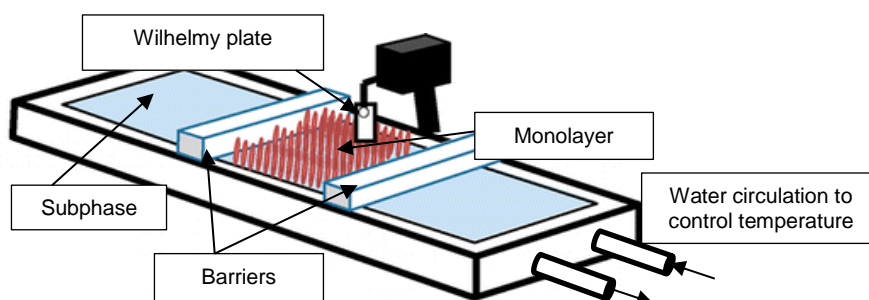
Figure 6 – Scheme of Langmuir Trough. (adapted from (Larsen, 2014))

The spreading of the substances in study can be performed with the aid of a spreading solvent, in which molecules to deposit are dissolved. Normally, in this technique, the required volume of spreading solution is applied using a micro syringe, drop by drop. After the application, it is required the solvent evaporation and after its disappearance, it leaves the film-forming molecules at the air/ aqueous

solution interface. Then a movable barrier is used to compress the monolayer, causing variation of the accessible area per molecule and thus, of the water surface tension. (Gaines, 1966)

The spreading solvent chosen should satisfy some requirements. (Gaines, 1966) The solvent must dissolve the molecules of the monolayer film and it must be chemically inert with respect to the subphase and the film material. High water solubility is to be avoided, since it can cause carriage of some monolayer forming material into the aqueous phase. Finally, it is desired to evaporate within a reasonable short time; however, very volatile solvents are not desired because its rapid evaporation prevents precise knowledge of solution concentration. The solvent chosen was chloroform, since it dissolves well the studied ILs and it is convenient as spreading solvent.

Spreading can be performed without a spreading solvent. (Gaines, 1966) The material, a small crystal or drop of the substance, is placed on the subphase, resulting in diffusion of the molecules over the liquid. The spreading will continue until the surface pressure reachs the *equilibrium spreading pressure* (ESP). This value represents the equilibrium between the monolayer film and bulk phase of the molecule. The drawback of such procedure is that the number of deposited molecule is unknown.

1.   Macroscopic Surface Pressure Measurements

The characteristic macroscopic description of a Langmuir monolayer is usually done using a surface pressure (π) vs area per molecule (A) isotherm measurement. This is the relationship between the surface pressure and the area occupied on the subphase liquid by the molecules of the film, given by the surface pressure-area curve (π-A). (Gaines, 1966) The value of surface pressure, π, at any A value is given by the next equation,

$$\pi(A) = \gamma_0 - \gamma(A)$$

<div align="right">Equation 1</div>

where γ and γ_0 are, respectively, the surface tensions of the film-covered subphase and bare subphase. The surface tension of pure water is high ($\gamma_0 = 72,8$ mN m^{-1} at T=18°C) and the spreading of a monolayer film on the subphase reduces the value of surface tension to a value of γ. Therefore, the value of π reflects the decrease of the surface tension of the subphase relatively to the surface tension of the pure water subphase.

Surface pressure was measured with a Wilhelmy System (Riegler & Kirstein, GmbH, Germany). The Wilhelmy method involves the measurement of the downward force (F) on a suspended plate (F=$\gamma \times (w + d) \times \cos\theta$). By maintaining the plate completely wet by the liquid, the contact angle (θ) is zero and then the surface tension is directly proportional to the force. Although an easy method, it is important to select the right plate material to diminish the deposition or absorption of molecules and to maintain the plate in a fixed position during all the experiment.
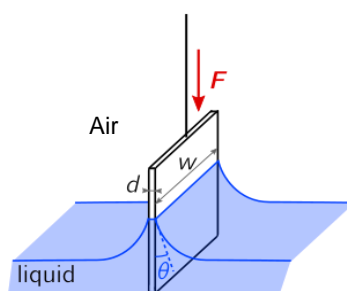
Figure 7 – Principle of Wilhelmy plate. (adapted from: (KYOWA Leading Answers, 2014)).

In Table 1 are listed the film-forming substances used in this work, their origin, reported purity and the concentration used in spreading solution; and the spreading solvent (chloroform) used in the solutions, its origin and reported purity. The through used has a compression ratio, i.e. ration between the maximum and minimum area, of 3.

Table 1 – Film-forming substances and spreading solvent used in this work, their origin, purity and concentration.

Name	Formula	Origin	Purity	Concentration	
				mmol/L	mg/mL
1-dodecyl-3-methylimidazolium bis(trifluoromethylsulfonyl)amide	$C_{18}H_{31}F_6N_3O_4S_2$	Iolitec	>98%	2.5	1.33
1-tetradecyl-3-methylimidazolium bis(trifluoromethylsulfonyl)amide	$C_{20}H_{35}F_6N_3O_4S_2$	Iolitec	>98%		1.40
1-hexadecyl-3-methylimidazolium bis(trifluoromethylsulfonyl)amide	$C_{22}H_{39}F_6N_3O_4S_2$	Iolitec	>98%		1.45
1-octadecyl-3-methylimidazolium bis(trifluoromethylsulfonyl)amide	$C_{24}H_{43}F_6N_3O_4S_2$	Iolitec	>98%		1.54
1-octadecyl-3-methylimidazolium chlorine	$C_{22}H_{43}ClN_2$	Iolitec	>98%		0.93
1-octadecyl-3-methylimidazolium hexafluorophosphate	$C_{22}H_{43}F_6N_2P$	Iolitec	>98%		1.20
Chloroform	$CHCl_3$	VWR Chemicals	G.C.	-	

II.2. Brewster Angle Microscopy (BAM)

Brewster Angle Microscopy (BAM) was first introduced in 1991. (Hénon & Meunier, 1991; Hoenig & Moebius, 1991) It is a technique that allows the visualization of Langmuir monolayers at air/ aqueous solution interface with 2 µm of image resolution.

This technique uses the unique angle at which no light is reflected from the air/ aqueous solution interface using *p*-polarized light. This angle is known as the Brewster angle for the material. Knowing that there is no reflection, the light is then transmitted. Brewster's angle can be derived from Snell's Law, knowing that the incident angle (θ_i) and the transmitted angle (θ_t) are complementary angles:

$$n_1 \sin \theta_i = n_2 \sin \theta_t \qquad \text{Equation 2}$$

$$\theta_t + \theta_i = 90° \qquad \text{Equation 3}$$

$$n_1 \sin \theta_i = n_2 \sin(90° - \theta_i) = n_2 \cos \theta_i \qquad \text{Equation 4}$$

$$\tan \theta_B = \frac{n_2}{n_1} \qquad \text{Equation 5}$$

where:

- n_1 and n_2 are the refractive index of the incident (air) and transmitting (subphase) medium, respectively;
- θ_i and θ_t are the incident and the transmitted angle, respectively;
- θ_B is the Brewster's angle (incident angle).

The Equation 5 is the Brewster's Law. For the air/ pure water interface, n_1=1 and n_2=1.33 (for visible light) and the Brewster's angle is 53°. With a constant angle, however, the addition of a monolayer on the water surface varies the Brewster's angle and then, reflection is observed on the layer covered part of the surface. Figure 8 illustrates the principle of Brewster angle microscopy.
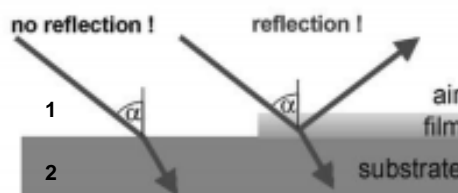
Figure 8 – Principle of Brewster angle microscopy. (adapted from: (Accurion-Solutions for Science, 2014))

In this technique, the contrast comes from the difference of the indeces between the bare subphase and the film-covered subphase. It is thus a technique that is well suited to observe phase transition regions where homogeneous dense phase domains coexist with low density regions.

The microscope that is used in this technique consists of a laser light source, a polarizing filter, an analyzer of the polarization state of the reflected beam and a camera detector. A simple BAM schematic is presented in Figure 9.
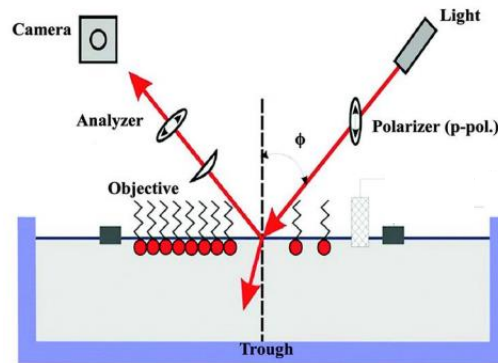
Figure 9 – Simple BAM scheme. (adapted from: (Benz, 2015))

II.3. X-ray Powder Diffraction (XRD)

X-Ray Powder Diffraction (XRD) is an x-ray diffraction technique used for characterizing materials and provides information of the organization at molecular or atomic length scales. (Pecharsky & Zavalij, 2009) The sample is in the powdery form, i.e. made of a large number of monocrystals randomly oriented, homogenized and when placed into a sample holder, it is necessary to assure a flat upper surface.

In this technique, the x-ray is usually generated using two different sources; by a cathode x-ray tube or by synchrotron radiation. The x-ray beam produced should be monochromatized, collimated to reduce dispersion and then directed toward the sample. When conditions satisfy Bragg's Law (Equation 6), constructive interferences are produced and therefore diffracted x-ray spots or peaks. The intensity of these diffracted x-ray is detected and recorded as a function of the scattering angle, the Bragg angle, 2θ, that is the angle between incident x-ray beam and detection direction. The positions and the intensities of the different peaks recorded are used to identify the structure of the material.

$$n\lambda = 2d\sin\theta \hspace{4cm} \text{Equation 6}$$

Where n is a positive integer and λ is the wavelength; d, the inter planar distance; and θ the incident angle.

II.4. Grazing Incidence X-ray Diffraction (GIXD)

Over the decades, conventional x-ray diffraction with large incident angles has been used to study the structure of bulk crystalline materials. (Dutta, 2000) X-ray allows the acquisition of microscopic structural information and study of the organization at molecular scale, thanks to its weakly interaction with the matter, deep penetration into material and wavelength adapted to the distance between atoms and molecules in crystals. Although, to study monolayers on the surface, it is necessary to limit x-ray illumination to the surface, therefore grazing incidence x-ray diffraction is needed.

Grazing Incidence X-ray Diffraction (GIXD) was originally developed in 1979. (Marra, Eisenberger, & Cho, 1979) In this technique, an incident angle smaller than the critical angle is used for total external reflection between two media with different indices of refraction ($n_{air}<n_{subphase}$). Like this diffraction can be made surface sensitive and no beam penetrates in the bulk. Only an evanescent wave propagates along the interface with an amplitude which exponentially decay along the vertical coordinate (the penetration depth of 4.6 nm at 8 keV).

In this technique, an incident x-ray beam strikes onto the surface at an angle smaller than the critical angle of total external reflection, creating an evanescent wave k_i (Figure 10). This wave is diffracted by the monolayer present in surface and the scattered/ diffracted wave is measured by the detector. The data can be collected varying 2θ to vary q_{xy} and varying $θ_z$, keeping 2θ constant, to vary q_z.
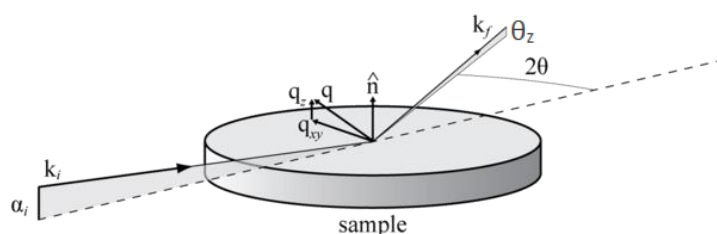
Figure 10 – Geometry of the GIXD experiment. (adapted from: (WikimediaFoundation, 2016))

Synchrotron radiation is important to use in this experiments, due to the mandatory use of evanescent wave in order to limit penetration of x-ray in the bulk. When evanescent wave is used very few photons interact with the surface, thus it is necessary a high flux which is possible when synchrotron radiation is used. This radiation is produced when charged particles, such as electrons, moving with relativistic speed, follows curved trajectories. (Gamboa, 2006; Mobilio & Balerma, 2003)

The GIXD experiments in the present project were carried out at SIRIUS beamline in Synchrotron facility SOLEIL in Orsay, France. The beamline is divided in source, optics and diffractometer. (Fontaine, Ciatto, Aubert, & Goldmann, 2014; SOLEIL Synchrotron, 2016)

The x-ray beam is produced by an Apple-II HU36 undulator source and provides photons in an energy range between 1.4 and 13keV. The optics aims to provide an incident beam adequate to the experiments. At a distance of 18.5 meters from the source, there is a double crystal monochromator (Si

111) to select the working energy (8 keV). Then, there is four mirrors: the first mirror, at 22 meters from the source, and the second one, at 26 meters, aim to achieve harmonic rejection and vertical focalization, moving themselves horizontal and vertically; a third one is optionally used for horizontal focalization; the last one is placed at 33 meters from the source to perform beam deflection for the liquid interface in study.

Lastly, there is the diffractometer at 35 meters from the source. This diffractometer has large interior space for samples environments. Collection of the scattered intensity was done on a very low noise, position sensitive, 1D gas detector, with 2048 channels on 150 mm. (SOLEIL Synchrotron, 2016)

This experimental setup makes possible the use of several detectors to study Langmuir films, such as the ones used on this project, GIXD and Total Reflection X-ray Fluorescence detectors.

II.5. Total Reflection X-ray Fluorescence (TRXD)

Total Reflection X-ray Fluorescence (TXRF) is a useful and versatile technique for chemical composition analysis of an interface. This technique can be performed simultaneously with GIXD, becoming a helpful technique to understand the system and the chemical composition of the interface.

X-ray Fluorescence is emitted when an excited electron drops from a higher energy atomic orbital to a lower one. The emitted energy is equal to the specific difference in energy between the two, starting and ending, quantum states of the electron. Since emitted energy is characteristic of a transition between specific electron orbitals in a particular element, the fluorescence spectrum can be used to detect elements that are present in the sample in study.

In contrast with conventional X-ray Fluorescence, this technique uses samples with smaller volumes, grazing incident angles as in GIXD and, moreover, detection limits of about a few femtograms (1 fg=10^{-15} g) can be achieved. (Görgl et al., 1997) In this project, TXRF was used as a complement of GIXD to study the composition of the interface. It measures the fluorescence coming from the x-ray irradiated volume. Using incidence angle, the penetration depth can be varied. The X-ray fluorescence detector used was a one-element, silicon drift detector (Brüker, Germany) equipped with a collimator. (SOLEIL Synchrotron, 2016; Wobrauschek, 2007)

III. Results and Discussion

In this chapter, it is going to be presented the results for every experiment made in this project: (π-A) isotherms, BAM and X-Ray Experiments (XRD, GIXD and TXRF).

III.1. Langmuir Isotherms

First, it was studied the stability of different substances at two different interfaces: air/ pure water and air/ salt water. For the salt water subphase, it was used 0.02 M of NaCl. All experiments were performed at 20°C; the deposited ILs solution volume used was 75 µL; three different relaxation times (solvent evaporation time and monolayer relaxation at low surface density) were used (10 minutes, one night and one weekend) as well as three different compression rates (20, 36 and 69 cm^2 min^{-1}; corresponding, respectively, to 0.0002, 0.0004 and 0.0008 nm^2 sec^{-1} $molecule^{-1}$). During the experiments, it was calculated the difference of areas between each compression, shown by the shift of the isotherm to smaller areas per molecule, called loss in area.

1.   [C_{18}mim][NTf_2]

Pure Water

First, the (π-A) isotherm of [C_{18}mim][NTf_2] at air/ pure water interface was studied for the three different relaxation times at low surface density and three different compression rates.

<u>10 minutes</u>. After deposition of the monolayer and 10 minutes for solvent evaporation, compression was then performed at a compression rate of 20 cm^2 min^{-1} (0.0002 nm^2 sec^{-1} $molecule^{-1}$) (ISOT1860).

Figure 11 shows the isotherm that represents the compression/ decompression cycles made. For the first compression (Figure 11 (a)), the isotherm shows a first increase of surface pressure over a large range of area per molecule (0.61 to 0.27 nm^2 $molecule^{-1}$), followed by an appearance of a plateau-like region at 24.0 mN m^{-1}. It is possible to consider that this monolayer is considerably compressed, due to the gradual increase in surface pressure up to 0.27 nm^2 $molecule^{-1}$. The plateau region, a highly compressible region, appears at small molecular areas (0.27-0.17 nm^2 $molecule^{-1}$). On first expansion (Figure 11 (b)), it is possible to see a shift of the isotherm shifted to smaller surface pressures/ molecular areas and a plateau also exists, but it appears at 14.5 mN m^{-1} and different molecular areas from the compression (0.22-0.35 nm^2 $molecule^{-1}$).

Figure 11 – ISOT1860 – Seven compression/ decompression cycles: (a) Compressions; and (b) Decompressions made. Isotherm performed at air/ pure water interface, after 10 minutes of solvent evaporation at a compression rate of 20 cm^2 min^{-1}.

Several compression/ decompression cycles were made to study the reproducibility of the (π-A) isotherm after more than one cycle. In the second and third compression, it is observed a decrease of the plateau size (0.22-0.17 nm^2 molecule^{-1} and 0.18-0.17 nm^{2}molecule^{-1}, respectively), that does not exist at the fourth; the highest pressure is reached in the third compression (24.3 mN m^{-1}). From the fourth to seventh compression, the maximum surface pressure reached decreases at each compression made. Although, the second and third expansion start at the same surface pressure and molecular area as the first expansion, it is observed a decrease of the plateau size ($\Delta A_{exp\ 2}$=0.06 nm^2 molecule^{-1} and $\Delta A_{exp\ 3}$=0.03 nm^2 molecule^{-1}) which appears only until third expansion, alike in compressions.

To study the effect of compression rate on the isotherm, two other isotherms were made with compression rates of 36 (ISOT18120) and 69 cm^2 min^{-1} (ISOT18240) (respectively, 0.0004 and 0.0008 nm^2 sec^{-1} molecule^{-1}) (Figure A 1 and Figure A 2, respectively).

Comparing to ISOT1860, all the compressions of ISOT18120 also present a gradual increase of surface pressure, followed by the appearance of a plateau, despite their shift to higher molecular areas/ surface pressures. The maximum surface pressure reached is higher, 26.5 mN m^{-1}, and it is reached at, the seventh compression. Although there is a decrease of plateau size as in ISOT1860, at each compression made, in ISOT18120 the plateau is bigger in size in all the compressions and it appears until the seventh compression, at least. On every expansion made, a plateau is seen at 15.0 mN m^{-1}, beginning at 0.20 nm^2 molecule^{-1}, approximately. The plateau size of each expansion is bigger than the correspondent plateau size of each expansion of ISOT1860, appearing at bigger molecular areas.

Regarding ISOT18240, its isotherms shifts to higher molecular areas than ISOT18120; all compression plateaus have bigger size than both ISOT1860 and ISOT18120, but the maximum surface

pressure, reached on the first compression, is lower than the value reached on the first compression of ISOT18120 (26.0 mN m⁻¹). ISOT18240 presents a major difference, relatively to the other two: two plateaus on first and second expansion. The first one appears on the beginning of the expansion, at 24.7 mN m⁻¹ and 0.17 nm² molecule⁻¹ ($\Delta A_{exp\,1}$=0.06 nm² molecule⁻¹; $\Delta A_{exp\,2}$=0.01 nm² molecule⁻¹); the second appears at 14.5 mN m⁻¹ and for the first compression at bigger areas than second compression (0.43-0.31 nm² molecule⁻¹ and 0.38-0.25 nm² molecule⁻¹, respectively). All the next expansions present a single plateau starting at 0.22 nm² molecule⁻¹ and at 14.5 mN m⁻¹.

The shift of the isotherms and the decrease of the plateau size and of the maximum surface pressure reached indicate a loss in area at each compression. In Table 2 are listed the loss in area at each compression, for every experiment made for [C₁₈mim][NTf₂].

Table 2 – Losses in area at each compression for the different isotherms at different pressures.

Isotherm	Pressure (mN m⁻¹)	Compression						
		2	3	4	5	6	7	8
ISOT1860	15	28%	38%	43%	48%	51%	56%	-
ISOTS1860	15	21%	29%	-	-	-	-	-
ISOT18120	15	21%	30%	35%	40%	43%	46%	48%
ISOTS18120	15	18%	26%	18%	19%	36%	38%	39%
ISOT18240	15	16%	23%	28%	32%	35%	38%	40%
ISOTS18240	15	18%	24%	28%	-	-	-	-
ISOT18N	10	10%	17%	22%	26%	-	-	-
ISOTS18N	10	13%	19%	-	-	-	-	-
ISOT18WE	8	4%	6%	12%	13%	15%	-	-
ISOTS18WE	8	11%	15%	23%	-	-	-	-
ISOT1660	6	41%	52%	-	-	-	-	-
ISOTS1660	6	33%	42%	50%	-	-	-	-
ISOT16120	1	-	29%	40%	46%	53%	58%	-
ISOT16120	3	43%	60%	65%	-	-	-	-
ISOTS16120	6	24%	32%	37%	41%	-	-	-
ISOT16240	3	31%	43%	52%	58%	63%	67%	69%
ISOTS16240	6	22%	28%	33%	36%	39%	41%	42%
ISOTS16N	6	11%	14%	18%	23%	-	-	-
ISOTS16WE	6	5%	7%	9%	12%	-	-	-

Night (N). The first compression was made after waiting one N (≈15 hours) at a compression rate of 20 cm² min⁻¹ (0.0002 nm² sec⁻¹ molecule⁻¹) and the isotherm (ISOT18N) is shown in Figure A 3.

Figure A 3 (a) shows the compressions done. Comparing with ISOT1860 (performed at the same solvent evaporation time and at the same compression rate), the first compression reaches a higher value of maximum surface pressure (23.8 mN m⁻¹) and all the isotherm shifts to smaller surface

pressures/ molecular areas and the plateau disappears, even in the first compression. In the following compressions, the isotherm does not show an increase of surface pressure until molecular area of 0.40 nm^2 molecule^{-1}, approximately, is reached. Afterward, it is observed a gradual increase of surface pressure over molecular area until it is reached its maximum value. Moreover, the isotherm dislocates to smaller values of surface pressure/ molecular areas with the compression, suggesting loss in area as in the isotherm after 10 minutes of solvent evaporation (Table 2, page 15).

At the expansions (Figure A 3 (b)) the isotherm shifts to smaller surface pressures/ molecular areas and it does not show any plateau.

Weekend (WE). For this molecule, the last Langmuir experiment was made after waiting one WE ($\approx$65hours) at a compression rate of 20 cm^2 min^{-1} (0.0002 nm^2 sec^{-1} molecule^{-1}) and the isotherm (ISOT18WE) is shown in Figure A 4. This isotherm shifts to even smaller surface pressures/ molecular areas than ISOT18N; therefore, the maximum surface pressure reached is the smallest for this compression rate, 13.0 mN m^{-1}. As with ISOT18N, the gradual increase of surface pressure is only observed when it is reached a value of molecular area of approximately 0.35 nm^2 molecule^{-1} in all the compressions. Both compression and expansion do not present plateau. Loss in area is shown in Table 2 (page 15).

Salt Water

[C$_{18}$mim][NTf$_2$] was also studied at air/ salt water interface. As in pure water, the molecule on this subphase was studied for three different relaxation times at low surface density and three different compression rates. Table 2 (page 15) shows the loss in area of each isotherm for this subphase.

10 minutes. After waiting 10 minutes for solvent evaporation, compressions were performed at three compression rates: 20 (ISOTS1860), 36 (ISOTS18120) and 69 cm^2 min^{-1} (ISOTS18240) (respectively, 0.0002, 0.0004 and 0.0008 nm^2 sec^{-1} molecule^{-1}). ISOTS1860, ISOTS18120 and ISOTS18240 are shown, respectively in Figure 12, Figure A 5 and Figure A 6. All of them show a similar behavior, which is comparable to the ones performed at air/ pure water interface: a gradual increase of surface pressure in the beginning of the compression, followed by an appearance of plateau at larger surface pressure. As in pure water, when the compression rate is increased, the isotherm shifts to higher molecular areas; and for an isotherm, at each compression made, there is a decrease of the plateau size and a shift of the isotherm to smaller molecular areas/ surface pressures. A plateau is visible at the beginning of each expansion (only 1st compression of ISOT1860), followed by a gradual decreasing of surface pressure.
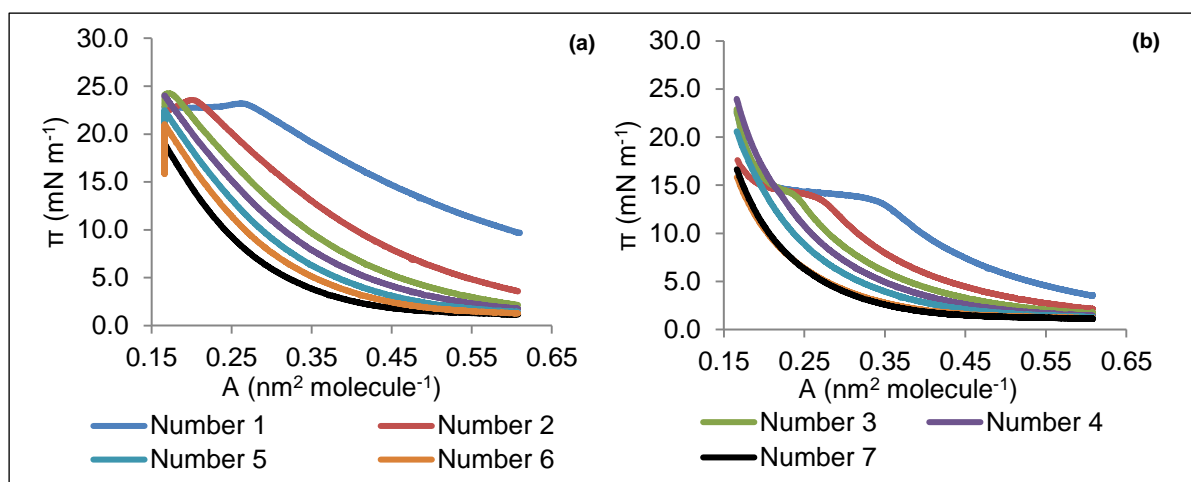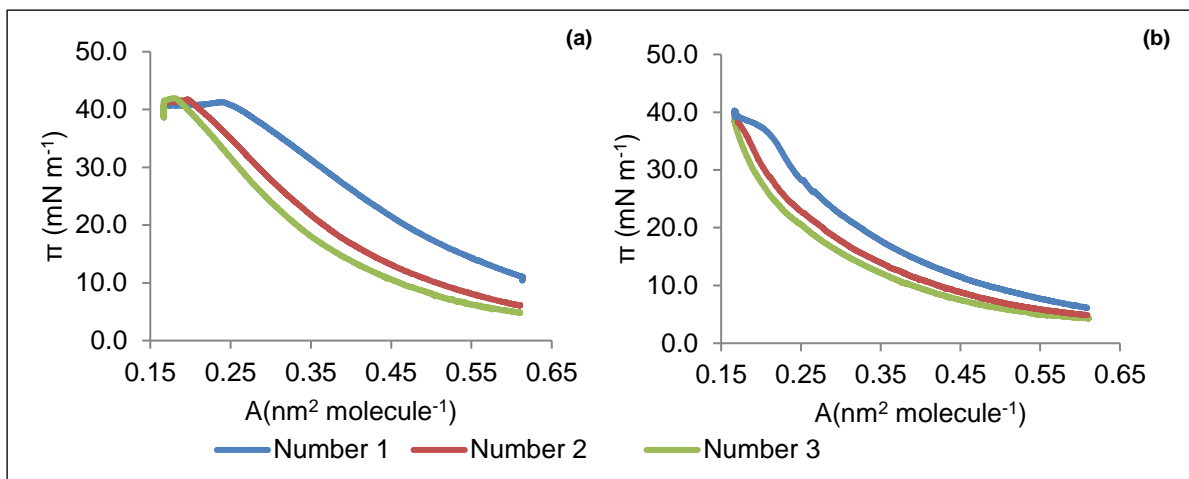
Figure 12 – ISOTS1860 – Three compression/ decompression cycles: (a) Compressions; and (b) Decompressions made. Isotherm performed at air/ salt water interface, after 10 minutes of solvent evaporation at a compression rate of 20 cm^2 min^{-1} (0.0002 nm^2 sec^{-1} molecule^{-1}).

<u>N.</u> After waiting one N for solvent evaporation, compression was performed at 20 cm^2 min^{-1} (ISOTS18N) (0.0002 nm^2 sec^{-1} molecule^{-1}) (Figure A 7). Although ISOTS18N shifts to smaller surface pressure/ molecular areas, its behavior is similar to those performed after 10 minutes of wait for solvent evaporation time: gradual increase of surface pressure followed by a plateau. In all the three compression/ decompression cycles made, a plateau is observed; the plateau present in the expansions begins always at the same surface pressure and molecular area.

<u>WE.</u> The last compression/ decompression experiment was performed at 20 cm^2 min^{-1} (0.0002 nm^2 sec^{-1} molecule^{-1}) after waiting one WE for solvent evaporation (ISOTS18WE) (Figure A 8).

Although this isotherm reaches similar maximum surface pressures, the maximum value is the smallest comparing to those performed at the same subphase. As in the air/ pure water interface, ISOTS18WE shifts to smaller surface pressures/ molecular areas than ISOTS18N and both compression and decompression do not present plateau.

When comparing loss in area at air/ pure water and air/ salt water interfaces, presented on Table 2 (page 15), it is shown that there is a bigger loss at the air/ pure water interface, therefore the addition of salt stabilizes the monolayer formed. Moreover, the maximum surface pressure reached is higher.

2. [C$_{16}$mim][NTf$_2$]

Regarding [C$_{16}$mim][NTf$_2$], it was performed all the same experiments done with [C$_{18}$mim][NTf$_2$], except for WE at air/ pure water interface.

Pure Water

As with the previous molecule, the first experiments were performed at air/ pure water interface They were performed for two different solvent evaporation times and three different compression rates.

10 minutes. Starting with experiments after waiting 10 minutes for solvent evaporation, compressions performed at three different compression rates: 20 (ISOT1660), 36 (ISOT16120) and 69 cm^2 min^{-1} (ISOT16240) (respectively, 0.0002, 0.0004 and 0.0008 nm^2 sec^{-1} molecule^{-1}) (Figure A 9, Figure A 10 and Figure A 11).

As [C$_{18}$mim][NTf$_2$], at each compression there is a shift of the isotherm to smaller surface pressure/ molecular areas, but contrary to [C$_{18}$mim][NTf$_2$], [C$_{16}$mim][NTf$_2$] does not form plateaus when compressed, not even at the first compression or at 69 cm^2 min^{-1} (0.0008 nm^2 sec^{-1} molecule^{-1}). The isotherm shows a gradual increase of surface pressure, which is observed at lower molecular areas at each compression made. The highest maximum surface pressure is reached on ISOT16240 (21.8 mN m^{-1}), but this value is lower than the maximum surface pressure of ISOT1860. The loss in area can be compared on Table 2 (page 15), confirming that [C$_{18}$mim][NTf$_2$] form more stable monolayers at this interface than [C$_{16}$mim][NTf$_2$].

N. Then it was performed experiments after waiting one N. Knowing that at each compression made, after waiting 10 minutes, there is a large shift of the isotherm to smaller surface pressures/ molecular areas, it was decided to test ISOT16N at three different compression rates (ISOT16N60: 20, ISOT16N120: 36 and ISOT16N240: 69 cm^2 min^{-1}; respectively 0.0002, 0.0004 and 0.0008 nm^2 sec^{-1} molecule^{-1}). Figure A 12 shows the three isotherms and it can be concluded that [C$_{16}$mim][NTf$_2$] is not stable after waiting one N for solvent evaporation since no surface pressure increase is observed during compression, regardless of the compression rate used. From this results, it was decided not to do the experiment after waiting a WE.

Salt Water

As said before at air/ salt water interface all the experiments done with [C$_{18}$mim][NTf$_2$] were also performed with [C$_{16}$mim][NTf$_2$].

10 minutes. The experiments performed after waiting 10 minutes for solvent evaporation at air/ salt water interface (ISOTS1660: 20, ISOTS16120: 36 and ISOTS16240: 69 cm^2 min^{-1}; respectively, 0.0002, 0.0004 and 0.0008 nm^2 sec^{-1} molecule^{-1}; Figure A 13, Figure A 14 and Figure A 15, respectively) present a similar behavior comparing to ISOT1660, ISOT16120 and ISOT16240: increase of surface pressure during all the compression; shift of the isotherm to smaller surface pressure/ molecular areas, at each compression; no plateau formation during compressions; and the highest maximum surface

pressure is reached on ISOTS16240 (31.8 mN m^{-1}). As the isotherms performed in the air/ pure water interface the surface pressure increase occurs at lower molecular areas at each compression made.

N. The experiment after waiting one N (ISOTS16N; Figure A 16) was made at 20 cm^2 min^{-1} (0.0002 nm^2 sec^{-1} molecule^{-1}). Despite the similar behavior comparing this isotherm to the one performed after 10 minutes of wait (at the same compression rate) the increase of surface pressure only occurs when it is reached 0.40 nm^2 molecule^{-1} for the first and 0.30 nm^2 molecule^{-1} for the following compressions and the maximum pressure of 13.4 mN m^{-1} is reached, on the first compression.

WE. The isotherm performed after one WE (ISOTS16WE; Figure A 17) at 20 cm^2 min^{-1} (0.0002 nm^2 sec^{-1} molecule^{-1}) has a similar behavior to the ones performed at the same subphase, however at the first compression the increase of surface pressure only occurs at 0.32 nm^2 molecule^{-1} and on the following ones at 0.30 nm^2 molecule^{-1} and the maximum pressure reached is 8.9 mN m^{-1}.

From the results it can be concluded that [C$_{16}$mim][NTf$_2$] are less stable than [C$_{18}$mim][NTf$_2$] on both subphases. It can be corroborated from the Table 2 (page 15), where it is shown that the loss in area for [C$_{16}$mim][NTf$_2$] is bigger when compressed (when the same conditions are used). Thus, it is demonstrated that with the decrease of the hydrophobic tail, the stability of the film decreases. The existence of the shift of the isotherm to smaller areas per molecule, i.e. loss in area, could suggest that the molecules are disappearing from the surface by dissolution in water.

3. [C$_{14}$mim][NTf$_2$] and [C$_{12}$mim][NTf$_2$]

Regarding air/ pure water interface, experiments were performed after 10 minutes: at the three compression rates, considered for the other molecules, for [C$_{14}$mim][NTf$_2$] (ISOT1460; Figure A 18, ISOT14120; Figure A 19 and ISOT14240; Figure A 20); and at 36 (ISOT12120) and 69 cm^2 min^{-1} (ISOT12240) (respectively, 0.0004 and 0.0008 nm^2 sec^{-1} molecule^{-1}) for [C$_{12}$mim][NTf$_2$] (Figure A 21). At air/ salt water interface, ISOTS1460, ISOTS14120 and ISOTS14240 were performed (Figure A 22, Figure A 23 and Figure A 24, respectively).

Pure Water

[C$_{14}$mim][NTf$_2$]. The first experiment made with this molecule was ISOT1460. At this compression rate, the compression of the film does not induce an increase of surface pressure; as opposed to when others rates are used, which shows an increase of surface pressure that begins at 0.25 nm^2 molecule^{-1} approximately. As in previous experiments, the highest surface pressure (2.4 mN m^{-1}) is reached when the fastest compression rate is used (69 cm^2 min^{-1}; 0.0008 nm^2 sec^{-1} molecule^{-1}), despite the values obtained for both compression rates (36 and 69 cm^2 min^{-1}; respectively, 0.0004 and 0.0008 nm^2 sec^{-1} molecule^{-1}) are not very different (1.6 and 2.4 mN m^{-1}, respectively). Both isotherms present a maximum surface pressure smaller than the value of surface pressure measured after spreading.

[C$_{12}$mim][NTf$_2$]. At this subphase, only ISOT12120 and ISOT12240 were performed, due to the fact that ISOT1460 did not show any variation when compressed. By the previous results, it was concluded that the molecule became less stable with the decrease of the hydrophobic tail, so no change will be expected during compression of this molecule, which happened.

Oppositely to [C$_{14}$mim][NTf$_2$] when [C$_{12}$mim][NTf$_2$] is compressed, no increase of surface pressure is observed, regardless of the compression rate used.

Salt Water

[C$_{14}$mim][NTf$_2$]. ISOTS1460 was the first isotherm performed at this interface. At this compression rate, the molecule shows a small increase of surface pressure when compressed for the first time and in the following compressions no increase is observed. Though it is observed an increase of surface pressure, the maximum surface pressure reached (3.5 mN m^{-1}) is smaller than the value measured after deposition of the film (6.1 mN m^{-1}).

At the compression rate of 36 cm^2 min^{-1} (ISOT14120; 0.0004 nm^2 sec^{-1} molecule^{-1}), it is observed an increase of surface pressure at the first compression (8.9 mN m^{-1}) and a smaller increase at the second one (3.3 mN m^{-1}), which is smaller than the value measured after deposition of the film (7.3 mN m^{-1}). At 69 cm^2 min^{-1} (ISOT14240; 0.0008 nm^2 sec^{-1} molecule^{-1}), it is observed an increase at the first three compressions. The pressure reached at the first compression (10.4 mN m^{-1}) is the highest value reached with this molecule; at the second and third compressions, the values reached are smaller (5.3 and 3.5 mN m^{-1}, respectively) than the value measured after spreading (6.4 mN m^{-1}).

By the results, it can be concluded that [C$_{14}$mim][NTf$_2$] and [C$_{12}$mim][NTf$_2$] are not stable at air/ pure water interface. Although, an increase of [C$_{14}$mim][NTf$_2$] stability at air/ salt water interface, this molecule is less stable than [C$_{18}$mim][NTf$_2$] and [C$_{16}$mim][NTf$_2$].

4. [C$_{18}$mim][Cl] and [C$_{18}$mim][PF$_6$]

The isotherms of [C$_{18}$mim][Cl] and [C$_{18}$mim][PF$_6$] were performed after 10 minutes at air/ pure water interface and at a compression rate of 20 cm^2 min^{-1} (0.0002 nm^2 sec^{-1} molecule^{-1}) (Figure A 25). Two compression/ decompression cycles were made for each molecule, during which both molecules showed a variation of surface pressure of 0.3 mN m^{-1} approximately, allowing to consider no variation during the process. Therefore, it can be concluded that both of these molecules do not form stable monolayers at this interface. Considering that [C$_{18}$mim][Cl] is soluble in pure water, the non-stability of this monolayer can be explained; and as well as, by the results, it can also be concluded that [C$_{18}$mim][PF$_6$] is soluble in pure water.

5. Equilibrium Spreading Pressure Measurements (ESP)

As said above, the ESP is defined as the equilibrium surface pressure between the film and its bulk phase. The bulk phase was placed on the subphase in study (pure or salt water) and π was monitored with time until it reached the saturation, the ESP value (example on Figure A 26). The ESP was measured at a constant area and all substances studied are solids, except [C_{12}mim][NTf$_2$], that is a liquid at working temperature. In Table 3, it is shown the ESP values for each substance and subphase studied.

Table 3 – ESP value measured for the different molecules at pure and salt water.

Molecule	ESP (mN m^{-1})	
	Pure Water	Salt Water
[C_{18}mim][NTf$_2$]	13.8	23.3
[C_{16}mim][NTf$_2$]	16.7	36.2
[C_{14}mim][NTf$_2$]	29.7	39.4
[C_{12}mim][NTf$_2$][1]	26.3	28.9
[C_{18}mim][Cl]	33.2	-
[C_{18}mim][PF$_6$]	34.0	-

From the results present in Table 3, it can be concluded that there is a correlation in both subphases between the value of ESP measured and the increase of the hydrophobic tail of the molecules (with the [NTf$_2$] anion): increasing the hydrophobic tail, the ESP value diminishes. The increase of the tail increases the hydrophobicity of the molecules leading the film-forming to spread fewer molecules into the surface affecting less the surface tension of the subphase, resulting in a lower value of surface pressure and, therefore, a lower ESP (Equation 1) value. As such [C_{18}mim][NTf$_2$] has the lesser value of ESP.

Because [C_{12}mim][NTf$_2$] has a smaller hydrophobic tail and the same anion, it would be expected to have a higher value for ESP, when compared to the value of [C_{14}mim][NTf$_2$]. However that does not happen since the molecule is a liquid and it can't be compared with the value measured for solid molecules, so [C_{12}mim][NTf$_2$] does not fit the correlation. Moreover, since this molecule has a smaller chain, dissolution can not be excluded.

Both [C_{18}mim][Cl] and [C_{18}mim][PF$_6$] are soluble so there is always absorption of the molecules present on the monolayer during the measurement, consequently the value measured is not an equilibrium value.

---

[1] Molecule Liquid.

6.   Equilibrium Isotherm

All the (π-A) isotherms made show a shift of the curves to smaller areas per molecule which can be attributed to the disappearance of the molecules by dissolution in the subphase or even irreversible crystal formation. However, it is not possible to confirm that this disappearance is complete. In order to confirm such hypothesis, for a fixed surface pressure, it was taken the measured values of area per molecule of each compression and then they were plotted along time. The experimental curve is then fitted with the function $A = A_0 + constant \times e^{\frac{constant}{t}}$. Since the constant A_0 is different from zero, it can be concluded that, if an infinite number of compressions/ decompressions were made, the isotherm would reach an "equilibrium isotherm" made of the (A_0, π) points. On Figure 13, the measured values of area per molecule of each compression in ISOT1860, for a surface pressure of 10.0 mN m^{-1}, are plotted along time; on Figure 14, there is plotted the correspondent equilibrium isotherm. On Figure 15 to Figure 23, there are the equilibrium isotherms for each of the other isotherms of [C$_{18}$mim][NTf$_2$], on both surfaces; on Chapter VI Appendix (from Table A 1 to Table A 10) there are the values of equilibrium area per molecule, A_0, for each fixed surface pressure, π, used to plot each equilibrium isotherms.
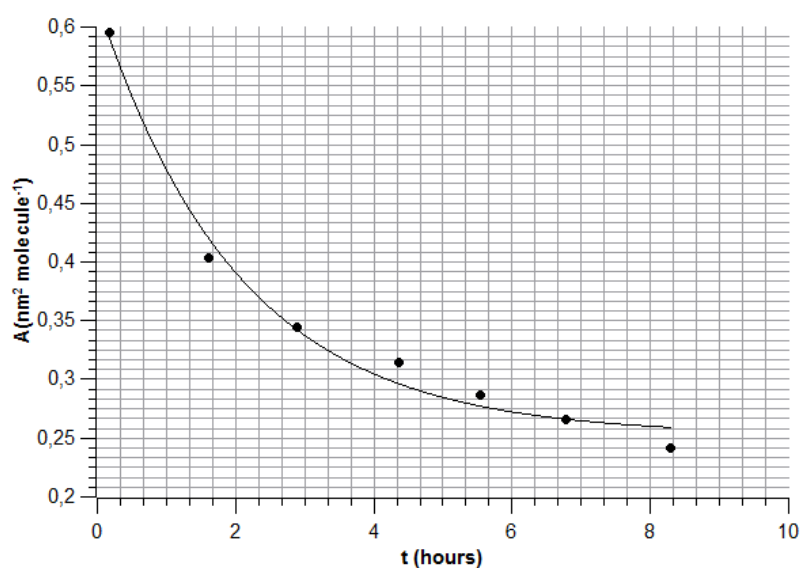
Figure 13 – Area per molecule vs time (hours), taken for a fixed surface pressure of 10.0 mN m^{-1}. Values taken from ISOT1860.
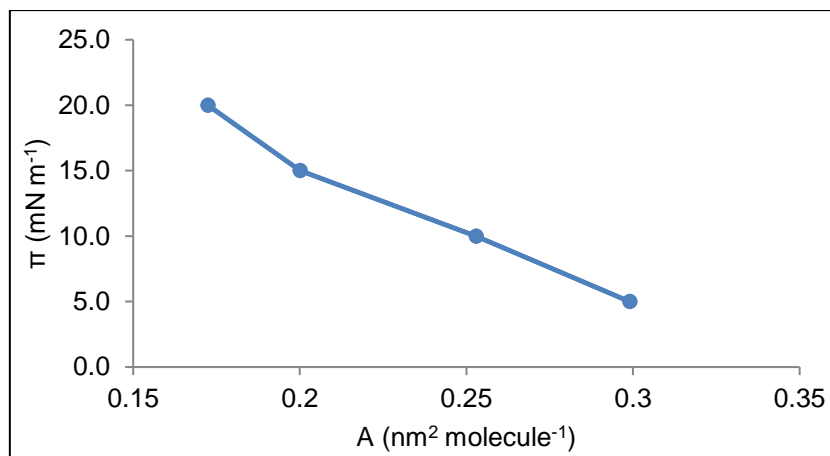
Figure 14 – Equilibrium isotherm of ISOT1860 ((π-A_0) curve).
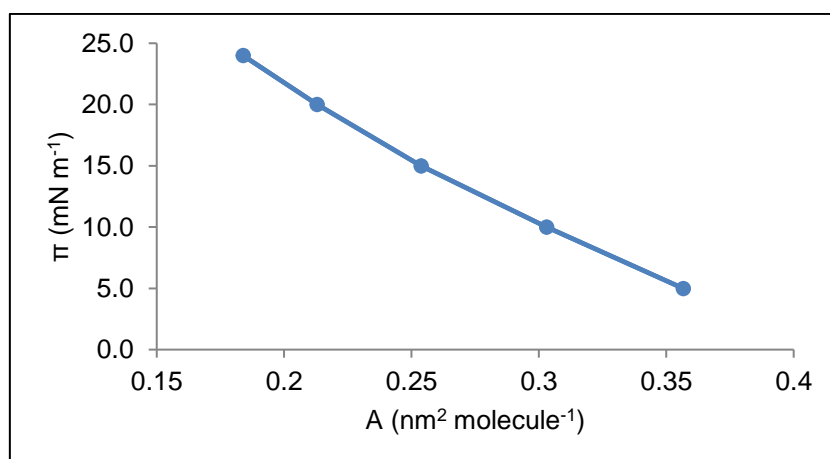
Figure 15 – Equilibrium isotherm of ISOT18120 ((π-A_0) curve).
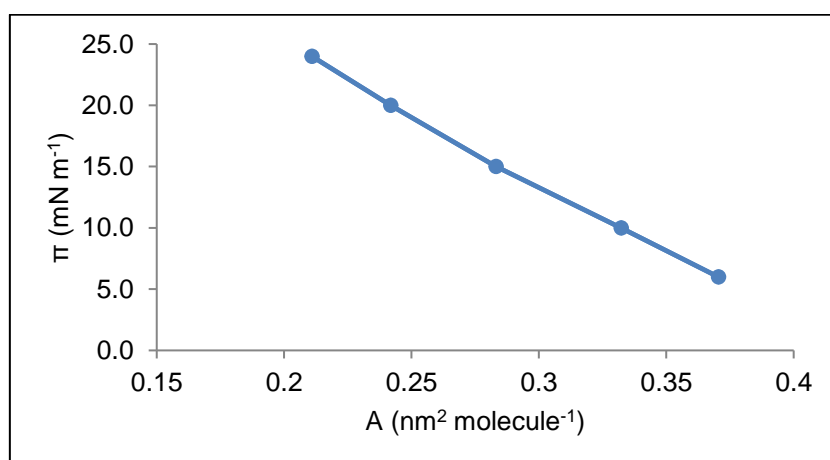
Figure 16 – Equilibrium isotherm of ISOT18240 ((π-A_0) curve).
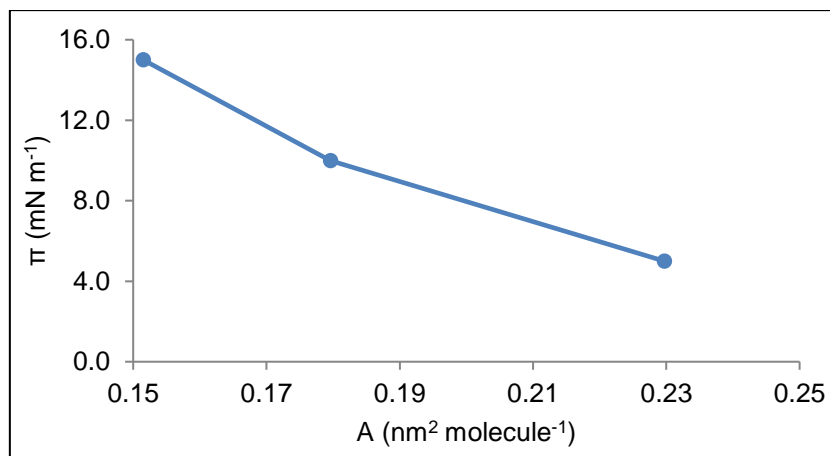
Figure 17 – Equilibrium isotherm of ISOT18N ((π-A_0) curve).
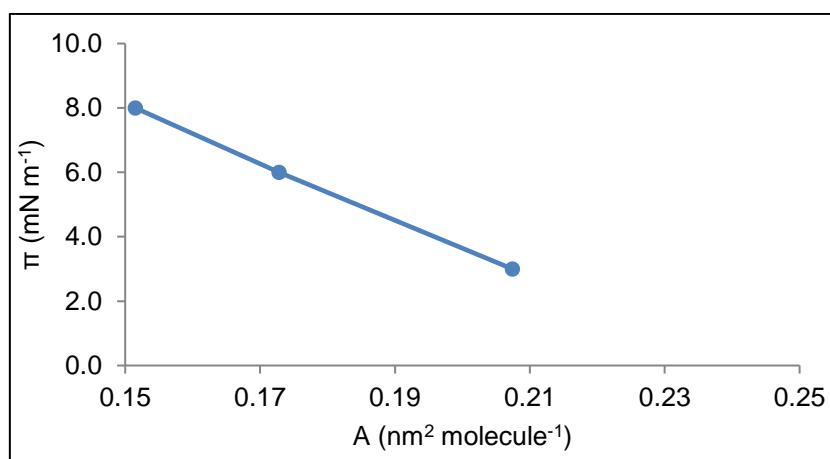
Figure 18 – Equilibrium isotherm of ISOT18WE ((π-A_0) curve).
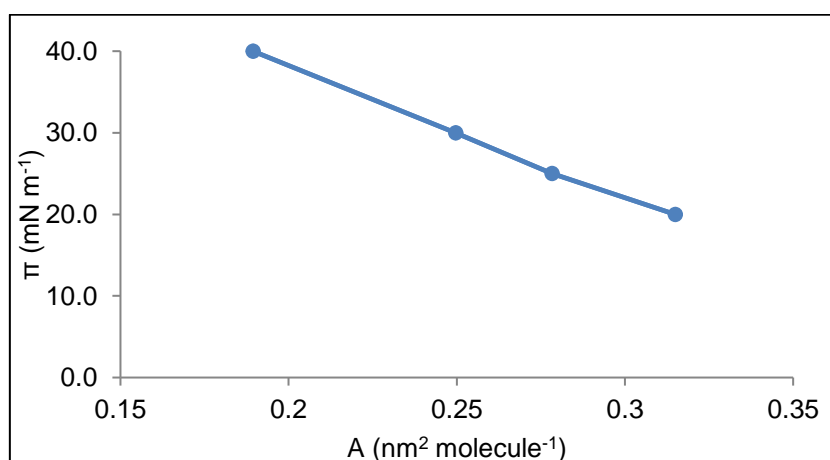
Figure 19 – Equilibrium isotherm of ISOTS1860 ((π-A_0) curve).
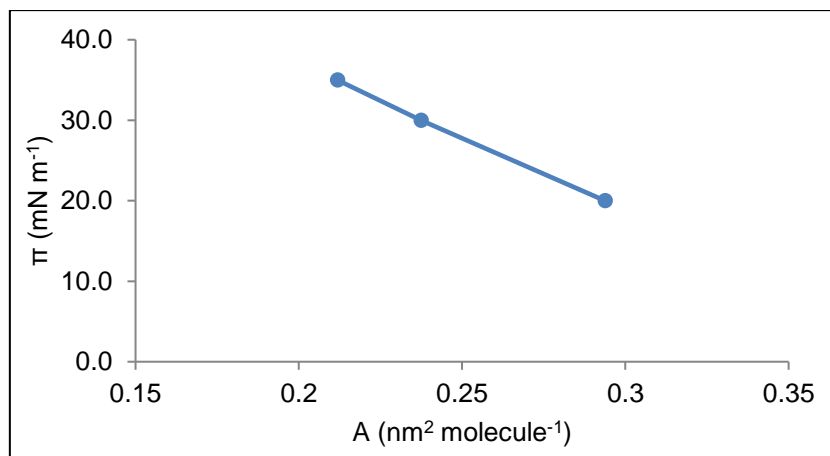
Figure 20 – Equilibrium isotherm of ISOTS18120 ((π-A_0) curve).
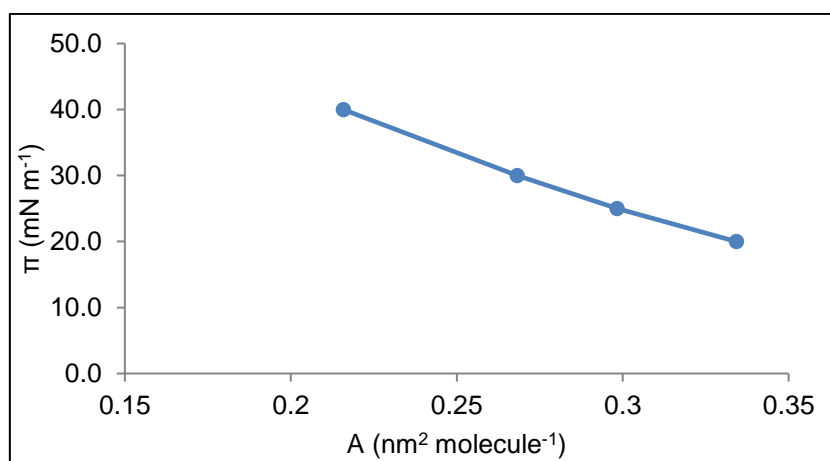
Figure 21 – Equilibrium isotherm of ISOTS18240 ((π-A_0) curve).
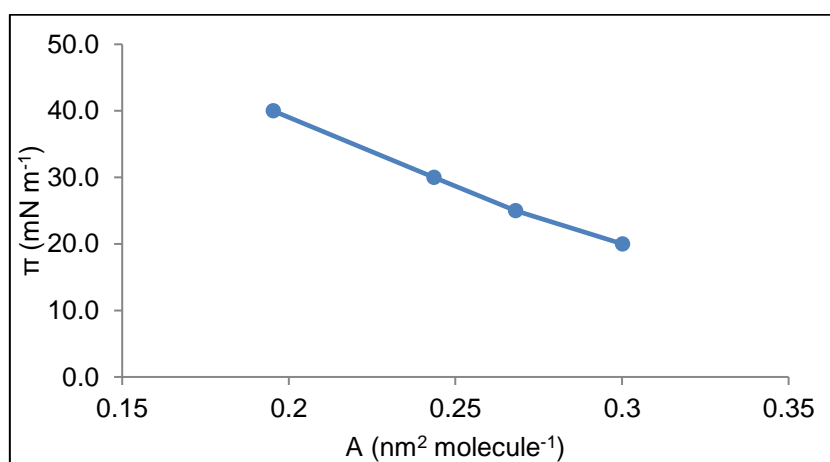
Figure 22 – Equilibrium isotherm of ISOTS18N ((π-A_0) curve).
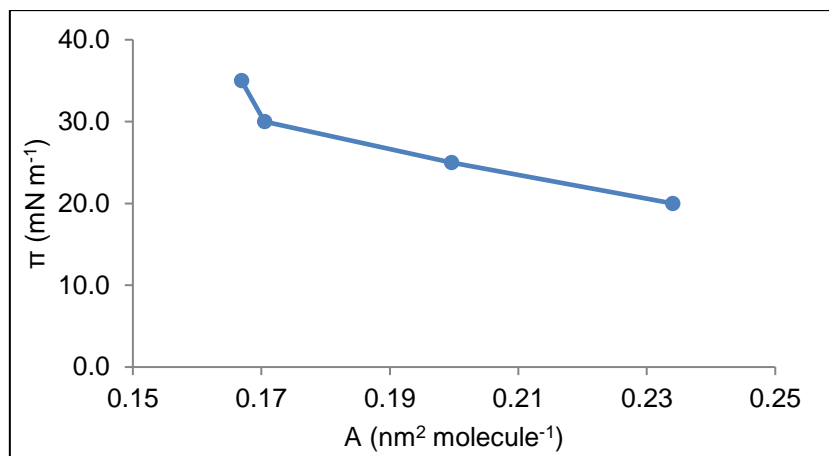
Figure 23 – Equilibrium isotherm of ISOTS18WE ((π-A_0) curve).

The existence of an "equilibrium isotherm" which limit area are around 0.17 nm^2 $molecule^{-1}$, close to the cross section of the hydrocarbon chain, suggests that the loss of area phenomenon is more complex than only molecule dissolution.

7. Conclusions of macroscopic measurements

As shown by the results above,

- The addition of NaCl to the water stabilizes the monolayer, increasing the surface pressure comparing to the isotherms performed at pure water, which can be proved by the following results:
    - The maximum pressure reached is higher at the air/ salt water interface;
    - It is more likely to find plateaus at air/ salt water interface rather than air/ pure water interface (ex.: ISOT18N vs ISOTS18N);
    - The loss in area per compression is larger at air/ pure water interface than at air/ salt water interface (Table 2; page 15);
- $[C_{18}mim][Cl]$ and $[C_{18}mim][PF_6]$ are not stable at air/ pure water interface;
- The stability of $[C_nmim][NTf_2]$ follows the same behavior as fatty acids (the higher the n, greater the stability):
    - On pure water subphase, $[C_{14}mim][NTf_2]$ proved to be not stable. On salt water subphase, the molecule showed a small enhance of stability;
    - Like $[C_{14}mim][NTf_2]$, $[C_{12}mim][NTf_2]$ does not form a stable monolayer on pure water subphase;
    - Although $[C_{18}mim][NTf_2]$ is the molecule that forms more stable monolayers, $[C_{16}mim][NTf_2]$ forming-films are also stable both on pure and salt water;
    - $[C_{18}mim][NTf_2]$ is the molecule with the lesser ESP value, supporting the statement that this molecule is the most stable of the ones studied;

The loss in area attributed to a loss of molecules by dissolution in the subphase at first sight seems to be more complex, as proven by the existence of an equilibrium isotherm.

The next experiments (BAM and X-Ray experiments) were performed just for [C$_{18}$mim][NTf$_2$] since it proved to be the molecule that forms more stable monolayers.

III.2. Brewster Angle Microscopy (BAM)

BAM technique was used to complement the results/ interpretations obtained with Langmuir Isotherms at a smaller length scale. BAM images were obtained of [C$_{18}$mim][NTf$_2$] at pure water and at salt water subphase along compression/ decompression cycles.

The BAM images was recorded for two different relaxation times at low surface density (10 minutes and one N). However, experiments for one N did not show any formation of structures or domains. Next, only experiment results for 10 minutes are present.

Pure Water
Figure 25 shows BAM images recorded at position on the (π-A) isotherm corresponding to the arrows in Figure 24. At large areas on the first compression, it was expected to find circular domains (Filipe et al., 2016), however no domains were detected (Figure 25 (a)). This can be due to a camera contrast problem that persisted during all the experiments (with salt water subphase included) causing poor contrast and, consequently, difficulty to observe existent domains.

On compression, it is observed that the brightness of the image increases uniformly. As the plateau is reached brighter spots are observed (Figure 25 (b)). Those spots are associated to crystalline-like or at least 3D (not monolayer) structures and indicates a thicker film. The structures observed are growing until the end of the plateau (Figure 25 (c)). Those structures can be attached to the formation of crystalline-like structures, as suggested before. (Filipe et al., 2016)

During all the expansion, the structures seem to vanish/ dissolve until no domain are visible. Those structures seem to be large structures vanishing, before the plateau is reached (Figure 25 (d)); then, it is possible to detect some structures fractured on the plateau, just until its end (0.36 nm^2 molecule^{-1}; Figure 25 (e)), when they completely fracture and only small circular domains are found on the surface (Figure 25 (f)). Afterwards, these small domains gradually disappear from the BAM image.

Then, a second compression was performed to study the film when compressed again. In the beginning of the compression, no domains are observed, but when it is reached the value of area of approximately 0.35 nm^2 molecule^{-1} small circular domain are found (Figure 25 (g)). When the plateau is reached, bigger domains are found, smaller in size than the ones found on the first compression (Figure 25 (h)). Although these domains were found, it is not possible to observe on the BAM images recorded. This can be due again to the poor camera contrast. Alternatively, it may be because these are less thick and dense than those found on first compression, which can cause less reflectivity of the light, resulting in poor contrast. During expansion, as on first compression, the domains get smaller and disappear.

Finally, the third and last compression just show small domains (smaller in size than the ones found during the second compression) (Figure 25 (i)). Those domains could be considered as some residual domains that did not disappeared before.

The existence of bright spots and thicker film suggests the existence of a monolayer in coexistence with multi-layered structures, on the first two compression/ decompression cycles. As said before, the alkyl side chains (hydrophobic tail groups) are oriented towards air, so it is preferable the formation of monolayers or trilayers comparing to the formation of bilayers or tetralayers. (Filipe et al., 2016) On all the compressions, the appearance of the domains only happened above the plateau present on the expansions.

In addition to the problem with camera contrast, the difficulty in obtaining images with noticeable features can be due the fact that the area recorded (500 μm x 700 μm) by the camera is small relatively to the total area of the Langmuir trough, resulting in an area not recorded. Since this area not registered were larger, some existing domains could not appear on the recorded area.

Figure 24 – ISOT1860 – Three compression/ decompression cycles at air/ pure water interface: (a) first compression/ decompression cycle; (b) first and second compression/ decompression cycle; and (c) first and second compression/ decompression cycle and third compression. The characters present on the curves correspond to the BAM images on Figure 25.

Figure 25 – BAM images of [C$_{18}$mim][NTf$_2$] at air/ pure water interface at various stages of the compression/ decompression cycles (the characters correspond to the arrows in Figure 24). Image resolution: 2 µm.

Salt Water

BAM images recorded for salt water subphase are present on Figure 27, that correspond to the arrows on Figure 26.

At the beginning of the first compression, no domains were observed (Figure 27 (a)). This can be due to the camera poor contrast or to absence of domains. However, by the obtained by Filipe *et al.* on pure water (Filipe et al., 2016) and since the addition of NaCl to the subphase stabilizes the monolayer, it was expected to observe the presence of domains. Though, since no literature exists for [C$_{18}$mim][NTf$_2$] on this specific subphase, it is not possible to confirm that domains are supposed to be found. As in pure water, the image gets brighter, along the compression. Due to the poor camera contrast causing an unclear image, it was not possible to identify when domains start to appear. However, when the plateau was reached, small circular domains were observed (Figure 27 (b)). These were in larger number but smaller in size than the ones that appeared on the second compression on pure water. Since the spreading of a monolayer onto salt water subphase can result in a monolayer where crystalline areas and dense agglomerates coexist (Park et al., 2008), it can be supposed that the crystalline areas could have less density than the small agglomerates. Despite the appearance, it was not observed the vanishing or fracture of these domains, during the expansion; although, on 0.36 nm^2 molecule^{-1} and 21.0 mN m^{-1} approximately (near ESP value), it was possible to see some structures (Figure 27 (c)), but the image was not very clear. From this point of expansion, no domains or structures were captured (Figure 27 (d)).

At second and third compressions, no domains were observed (Figure 27 (e)); nonetheless, the domains that may exist on the second compression could be very small and difficult to observe due to camera resolution or due to low reflectivity of the domains.

As on pure water subphase, it is suggested the existence of a multi-layered structures on the salt water subphase by the results obtained. The difficulty to observe the domains/structures in any of the compressions may be due to a combination of several reasons: (i) poor camera contrast and low camera resolution; (ii) very small domains or domains less thick and dense than the ones recorded; and (iii) small area recorded compared to the Langmuir trough area.
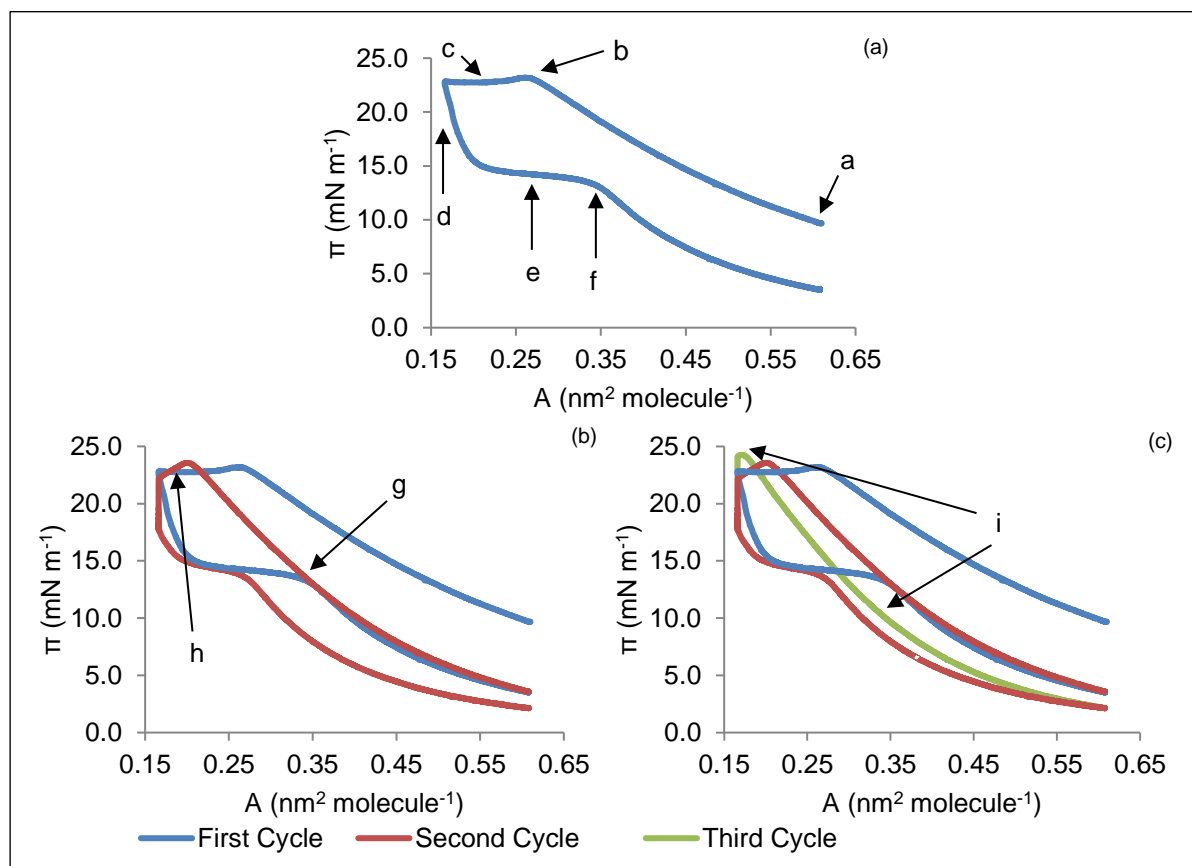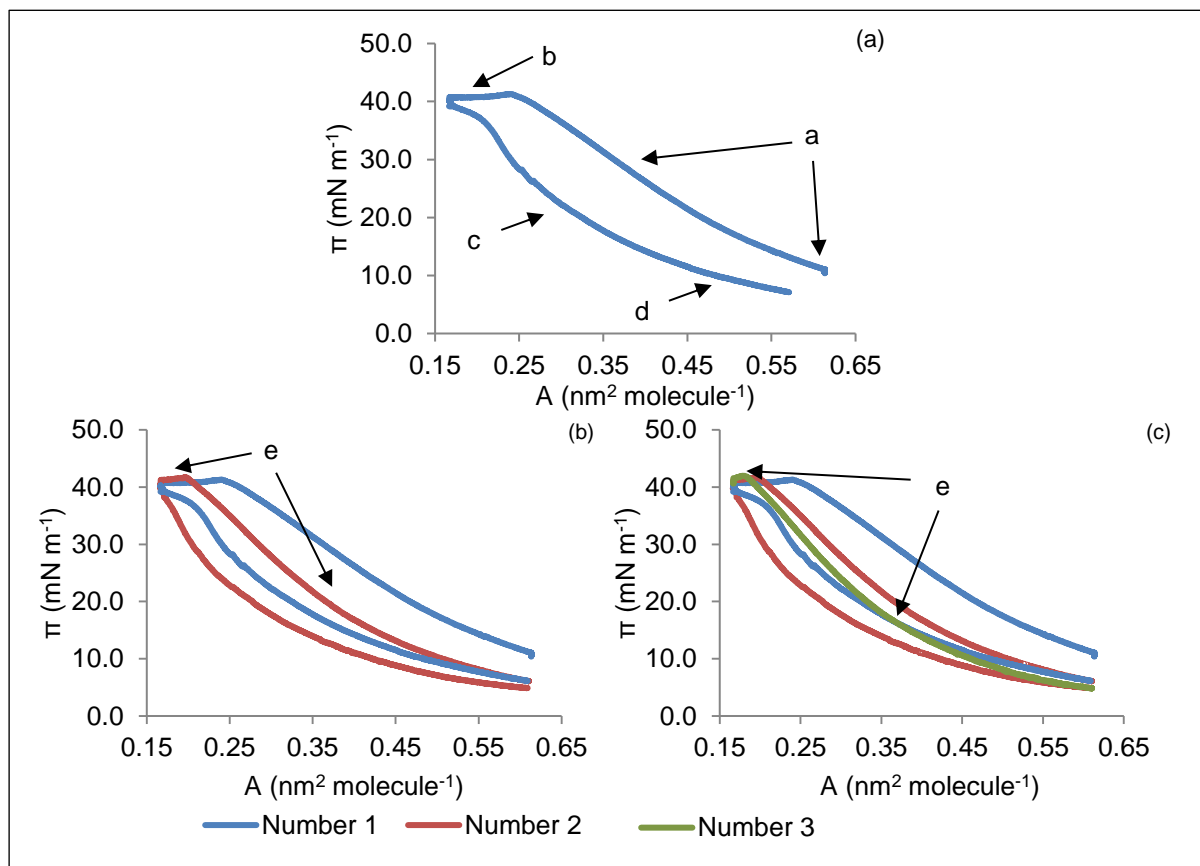

Figure 26 – ISOTS1860 – Three compression/ decompression cycles at air/ salt water interface: (a) first compression/ decompression cycle; (b) first and second compression/ decompression cycle; and (c) first and second compression/ decompression cycle and third compression. The characters present on the curves correspond to the BAM images on Figure 27.
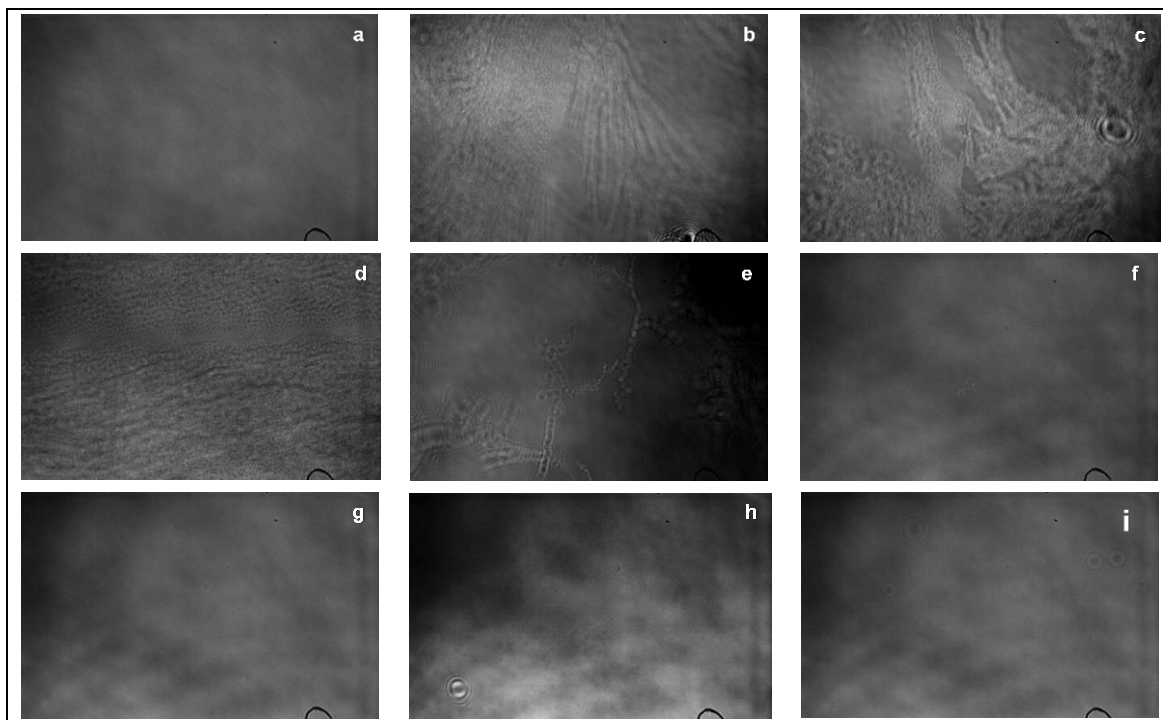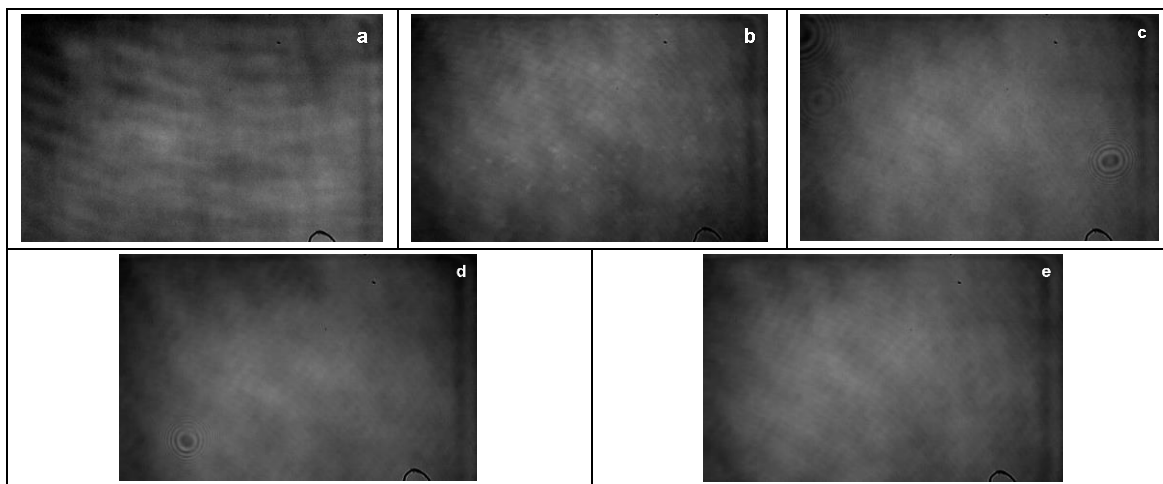
Figure 27 – BAM images of [C_{18}mim][NTf$_2$] at air/ salt water interface at various stages of the compression/ decompression cycles (the characters correspond to the arrows in Figure 26). Image resolution: 2 μm.

III.3. X-ray Experiments

1. Grazing Incidence X-ray Diffraction (GIXD) and X-ray Powder Diffraction (XRD)

[C_{18}mim][NTf$_2$] Langmuir monolayer was also studied at molecular level by GIXD. Due to the non-stability of the films at high surface pressures, the films were continuously compressed during each x-ray scan. The diffraction peaks from GIXD scan for the molecule were fitted with Lorentzian line shapes. This experiment was used to study the monolayer on pure water, for one compression/ decompression cycle (Table 4) and for three compression/ decompression cycles (Table 5) and on salt water along an isotherm (Table 7; page 35).

First, it was studied the molecule on pure water along the first compression. Since it was not known where were expected to find peaks, the GIXD scans were taken on different intervals: experiment 1 in the interval between $Q_{xy}=13.00$ nm^{-1} and $Q_{xy}=18.00$ nm^{-1}; the 2nd and 3rd between $Q_{xy}=13.00$ nm^{-1} and $Q_{xy}=16.50$ nm^{-1}; and the 4th in the interval of $Q_{xy}= 7.00$ - 8.20 nm^{-1}. It was performed four experiments at different volumes, compression rates and relaxation times (Table 4). From those experiments, it was possible to conclude that there are at least four peaks in the powder patterns for each value of inverse surface density, $Q_{xy}=7.60$ nm^{-1}, $Q_{xy}=14.90$ nm^{-1}, $Q_{xy}=15.10$ nm^{-1} and $Q_{xy}=15.30$ nm^{-1}.

Then, the monolayer was studied for the next compressions (three compression/ decompression cycles; Table 5). The intervals for the next experiments were chosen taking into account the value of the peaks obtained before: 5th and 7th experiments were taken between $Q_{xy}=11.00$ nm^{-1} and $Q_{xy}=17.00$ nm^{-1}; and 6th in the interval $Q_{xy}= 11.00 – 14.50$ nm^{-1}. The peak $Q_{xy}=15.30$ nm^{-1} was only found on 2nd and 3rd compressions (7th experiment), though this has been the only peak that was found in all the experiments. On the first compression/ decompression (5th and 6th experiment) as well as on the other compressions, other peaks were found, $Q_{xy}=11.90$ nm^{-1}, $Q_{xy}=12.20$ nm^{-1}, $Q_{xy}=12.70$ nm^{-1} and $Q_{xy}=12.90$ nm^{-1}.

Table 4 – Diffraction peaks derived from GIXD scan of [C$_{18}$mim][NTf$_2$] on pure water subphase along the first compression. Incident energy: 8 keV.

Experiments	Volume used (μL)	Compression rate (cm² min⁻¹)	Relaxation time (min)	A (nm² molecule⁻¹)	π (mN m⁻¹)	Scattering Intensity	Q$_{xy}$ (nm⁻¹)	Width of the peaks (nm⁻¹)
1				0.56	15.0	73	15.09	1.29×10^{-1}
2	82	31	10	0.15	24.5	144	14.86	5.59×10^{-1}
				0.15	18.0	81	15.09	2.03×10^{-1}
				0.15	15.0	114	15.09	2.14×10^{-1}
3	82	26	16	0.15	26.0	75	15.32	1.55×10^{-1}
4	79	31	12	0.16	22.3	3	7.64	1.76×10^{-2}
						13	7.68	5.13×10^{-2}

Table 5 – Diffraction peaks derived from GIXD scan of [C$_{18}$mim][NTf$_2$] on pure water subphase along three compression/ decompression cycles. Incident energy: 10.5 keV.

Subphase	Volume used (μL)	Compression rate (cm² min⁻¹)	Compression or Relaxation time (min)	A (nm² molecule⁻¹)	π (mN m⁻¹)	Scattering Intensity	Q$_{xy}$ (nm⁻¹)	Width of the peaks (nm⁻¹)
5			1st comp after 10 min	0.35	21.0	8	12.15	8.60×10^{-2}
						8	11.97	1.06×10^{-1}
6				0.29	24.0	17	11.97	5.71×10^{-2}
						13	12.22	9.25×10^{-2}
						20	12.90	1.17×10^{-1}
			1st exp	0.15	15.5	7	12.23	1.01×10^{-1}
						1615	12.66	1.03×10^{-5}
7	75	20	2nd comp	0.17	16.4	12	11.99	6.50×10^{-2}
						9	12.21	4.95×10^{-2}
						7	15.30	6.34×10^{-2}
			3rd comp	0.20	24.5	5	12.29	1.26×10^{-1}
						5	15.32	2.68×10^{-2}
				0.17	16.8	14	12.20	1.94×10^{-1}
						1969	15.32	1.72×10^{-5}
				0.17	15.7	6	15.31	7.48×10^{-2}
				0.17	15.1	5	11.98	8.14×10^{-2}
						5	15.29	7.20×10^{-2}
				0.17	14.5	13	11.99	3.98×10^{-2}
						23	12.22	8.34×10^{-2}
						10	15.30	5.21×10^{-2}

The striking point of these data (Table 4 and Table 5) is that all the peaks found were obtained above the ESP value (13.8 mN m^{-1}) and no peaks were found below this value (Figure 28).
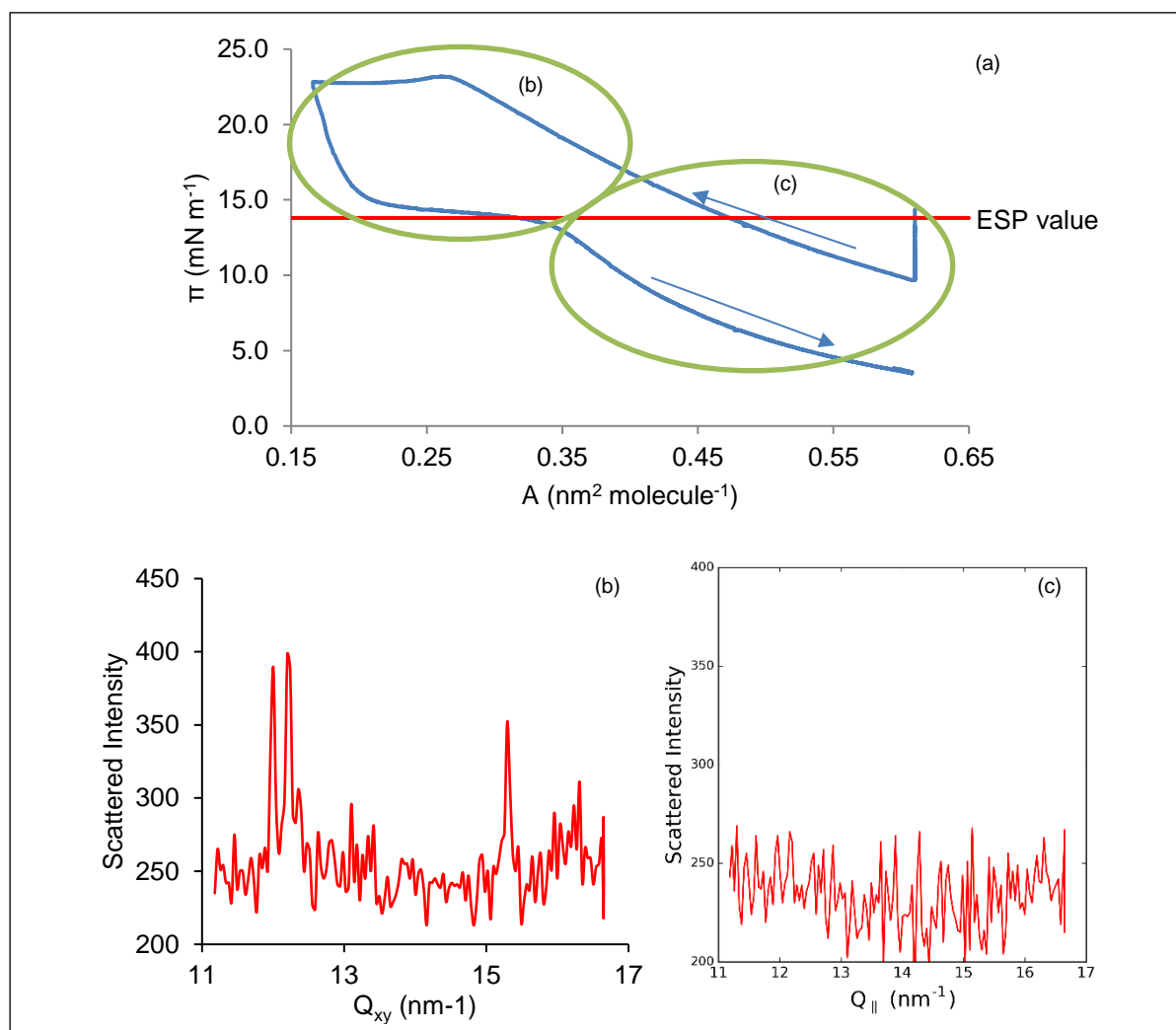
Figure 28 – GIXD spectrums obtained above (b) or below (c) the ESP on ISOT1860 (a). Note that $Q_{||}=Q_{xy}$.

From GIXD, besides the peaks obtained above, it is also obtained a Q_z - Q_{xy} map of the diffraction data (Figure 29 (b)). This map shows that the diffraction along Q_z, i.e. vertically, does not looks like 2D diffraction but to powder or multilayer diffraction. Indeed, some peaks looks like part of diffraction rings (3D powder) and some other are narrow in Q_z (multilayers). In addition to GIXD, it was also performed XRD of [C_{18}mim][NTf$_2$] on bulk form, using an wavelength of 1.18 Å. From the results of the experiments (Table 6) it can be concluded that some peaks obtained are coincident with the ones obtained by GIXD on pure water subphase and both scans are similar (Figure 30). These peaks show that the measured diffraction at pure water surface comes from 3D crystals or from multilayer formed at the air/ pure water interface upon compression, as showed by the Q_z - Q_{xy} map of the diffraction data.
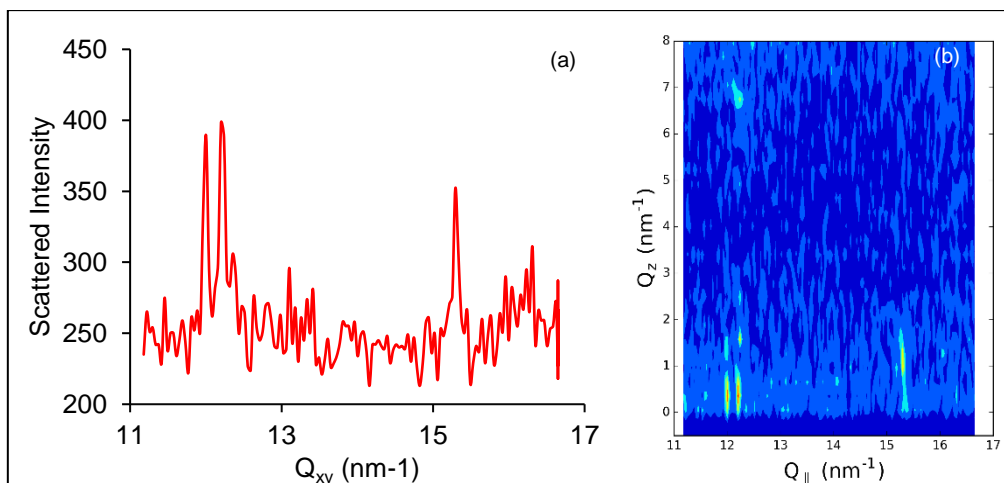
Figure 29 – GIXD spectrum: (a) Scattered Intensity vs Q_{xy} and (b) Qz vs $Q_{\parallel}$. Note that $Q_{\parallel}=Q_{xy}$.

Table 6 – Peaks obtained from XRD of [C_{18}mim][NTf$_2$].

						Q_{xy} (nm^{-1})						
12.10	12.30	12.40	12.50	13.10	13.80	14.10	14.80	15.30	15.40	15.70	15.80	16.50
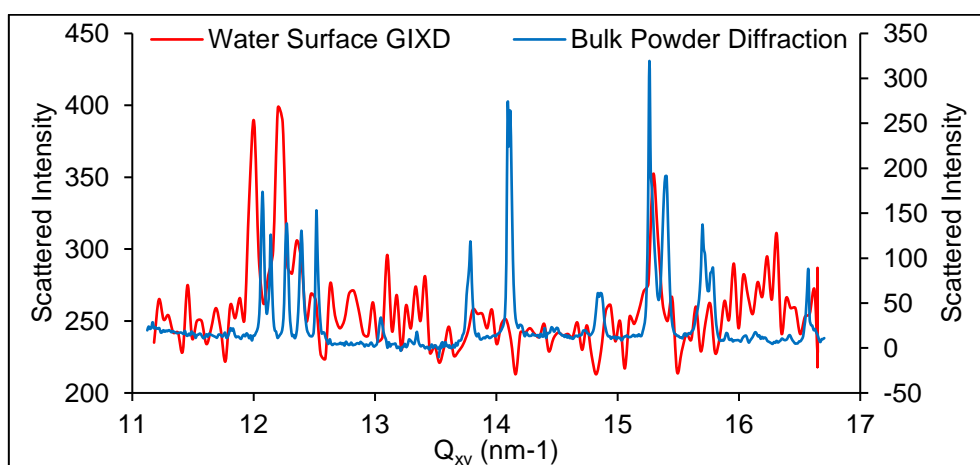
Figure 30 – Comparison of Bulk XRD (**blue**) and Water Surface GIXD (**Red**) Scans.

After, it was performed GIXD on salt water subphase. As on the previous experiments, it was performed several experiments (from 8 to 21) at different volumes, compression rates and relaxation times (Table 7). The intervals of the scans were similar to the intervals chosen on pure water subphase experiments: the 8th, 10th, 12th, 14th, 16th, 18th, 20th and 21st experiments were taken between $Q_{xy}=13.00$ nm^{-1} and $Q_{xy}=18.00$ nm^{-1}; the 9th and 11th in the interval of $Q_{xy}=9.00$ nm^{-1} and $Q_{xy}=17.00$ nm^{-1}; the 13th between $Q_{xy}=5.50$ nm^{-1} and $Q_{xy}=8.00$ nm^{-1}; and the other three (15th, 17th and 19th) from $Q_{xy}=7.00$ nm^{-1} to $Q_{xy}=8.60$ nm^{-1}.

As stated above on Chapter III.1 Langmuir Isotherms, the addition of NaCl to the pure water stabilizes the monolayer and consequently it was expected to find more peaks than the ones found on pure water subphase, which happens: the double number of the peaks found on the previous experiment (8) were found in this experiment (16)(Table 8). It was found 3 peaks between 7.40 nm^{-1} and 8.00 nm^{-1} at salt water subphase, comparing to pure water subphase, where only one peak was found on this interval; on salt water subphase, no peaks were found below 13.02 nm^{-1} and four peaks were found above 15.30 nm^{-1} (on pure water, four peaks were found below 13.0 nm^{-1} and no peaks were found above 15.30 nm^{-1}); the other nine peaks were found between 13.20 nm^{-1} and 15.30 nm^{-1}, comparing to two found on pure water. Four of these were only found on 3rd expansion: Q_{xy}=14.10 nm^{-1}, Q_{xy}=14.80 nm^{-1}, Q_{xy}=14.90 nm^{-1} and Q_{xy}=16.50 nm^{-1}. All the peaks on this subphase were found above the ESP value obtained for this subphase (23.3 mN m^{-1}).

Table 7 – Diffraction peaks derived from GIXD scan of [C$_{18}$mim][NTf$_2$] on salt water subphase along a typical isotherm. Incident energy: 8 keV.

Subphase	Volume used (µL)	Compression rate (cm² min⁻¹)	Relaxation time (min)	A (nm² molecule⁻¹)	π (mN m⁻¹)	Scattering Intensity	Q_{xy} (nm⁻¹)	Width of the peaks (nm⁻¹)
8	82	26	1st comp after 20 min	0.20	38.5	28	13.56	2.37×10⁻²
						11	14.74	4.28×10⁻²
						6	15.45	4.62×10⁻²
				0.15		23	13.59	2.78×10⁻²
						10	14.77	4.44×10⁻²
						5	15.48	2.70×10⁻²
9				0.15	35.9	15	13.59	2.95×10⁻²
						6	14.78	1.39×10⁻²
						11	15.08	9.50×10⁻²
10					33.3	7	13.58	2.05×10⁻²
				0.15	32.0	15	13.59	2.95×10⁻²
						6	14.78	1.39×10⁻²
						11	15.08	9.50×10⁻²
					30.0	2715	13.24	9.23×10⁰
						72	15.04	2.45×10⁻¹
						3	16.23	1.92×10⁻²
11					27.0	125	15.07	3.48×10⁻¹
12	70	26	1st comp after 30 min	0.29	38.0	427	13.72	2.41×10⁰
				0.20	37.0	60	13.59	2.53×10⁻²
13				0.15	35.6	34	7.39	1.83×10⁻²
						28	7.74	2.50×10⁻²
14						26	14.76	3.26×10⁻²
						69	15.08	3.84×10⁻²
						22	15.47	4.37×10⁻²
15				0.39	30.0	41	7.97	2.73×10⁻¹

Table 7 – Diffraction peaks derived from GIXD scan of [C18mim][NTf2] on salt water subphase along a typical isotherm. Incident energy: 8 keV.

Subphase	Volume used (µL)	Compression rate (cm² min⁻¹)	Relaxation time (min)	A (nm² molecule⁻¹)	π (mN m⁻¹)	Scattering Intensity	Q_{xy} (nm⁻¹)	Width of the peaks (nm⁻¹)
16	80	26	1st comp after 30 min	0.47	25.0	10	14.79	3.42×10^{-2}
16				0.47	25.0	13	16.27	5.14×10^{-2}
17				0.47	25.0	56	7.39	2.97×10^{-2}
17				0.47	25.0	42	7.74	3.70×10^{-2}
18				0.39	34.0	55	13.58	3.18×10^{-2}
18				0.39	34.0	57	14.77	4.50×10^{-2}
18				0.39	34.0	200	15.12	2.25×10^{-1}
18				0.39	34.0	33	15.47	6.16×10^{-2}
18				0.39	34.0	46	16.25	4.21×10^{-2}
18				0.39	34.0	7	15.50	3.49×10^{-2}
19				0.15	33.5	45	7.38	2.70×10^{-2}
19				0.15	33.5	27	7.74	3.21×10^{-2}
20				0.15	32.2	36	13.59	3.62×10^{-2}
20				0.15	32.2	19	14.76	5.70×10^{-2}
20				0.15	32.2	52	15.11	1.97×10^{-1}
20				0.15	32.2	13	15.47	5.85×10^{-2}
20				0.15	32.2	25	16.24	5.01×10^{-2}
21	70	31	3rd Comp²	0.19	38.0	4	13.58	3.02×10^{-2}
21			3rd Exp²	0.19	38.0	239	14.12	2.51×10^{-0}
21				0.19	38.0	33	15.08	1.91×10^{-1}
21				0.17	40.0	136	14.90	4.99×10^{-1}
21				0.17	40.0	51	16.51	2.05×10^{-1}
21				0.15	40.0	99	14.77	7.22×10^{-1}
21				0.15	35.0	174	14.80	1.08×10^{-0}
21				0.15	27.0	93	14.93	4.54×10^{-1}

Table 8 – Summary of the peaks found from GIXD on both subphases studied.

Q_{xy} (nm⁻¹)													
Interval	Pure Water				Salt Water								
7.4-8.0	7.6	-	-	-	7.4	7.7	8.0	-	-	-	-	-	-
Below 13.2	11.9	12.2	12.7	12.9	-	-	-	-	-	-	-	-	-
13.2-15.3	14.9	15.1	15.3	-	13.2	13.6	13.7	14.1	14.7	14.8	14.9	15.0	15.1
Above 15.3	-				15.4	15.5	16.2	16.5	-	-	-	-	-

---

² First compression after 20 minutes.

2. Total Reflection X-ray fluorescence (TRXF)

TRXF was used to analyse the chemical composition of the monolayer of [C$_{18}$mim][NTf$_2$] at the interface since this technique is chemically sensitive. The measurement consists in recording a fluorescence spectrum, i.e. the number of photons for each energy in the x-ray range coming from the illuminated interface. The fluorescence spectrum can give a lot of information which can characterize the excitation source (position of elastic and inelastic scattering lines) and the samples. All the chemical elements present in the sample influence and contribute to the resulting spectrum.

In the present work, it was analyzed the sulfur content, since it is present in [NTf$_2$]$^-$, during a three day experiment by its fluorescence energy emission (characteristic emitted energy of sulfur: 2.3 keV). This is possible because the peak intensity depends on the amount of the atom present on the analyzed volume. (Beckhoff, Kanngießer, Langhoff, Wedell, & Wolff, 2006; Haschke, 2014) The sulfur fluorescence intensity was normalized with the elastic fluorescence intensity, representing the number of photons used for excitation.

Besides being emitted, the incident x-ray light can be scattered by electrons. The two most significant types of scattering are elastic (Rayleigh) and inelastic (Compton) scattering. Light scattered by elastic scattering, i.e. without loss of energy of the scattered x-ray but with direction of propagation modified, has the same wavelength as the incident x-ray; whereas inelastic scattering has an increased wavelength (decrease of the energy), which happens when an x-ray photon hits an electron, transferring its energy. (Beckhoff et al., 2006; Haschke, 2014) Both elastic and inelastic peaks depend on the incident x-ray. The Compton peaks appear at slightly lower energy than the Rayleigh peak on the fluorescence spectrum, so they are fitted at the left side of the curve; whereas the elastic is fitted at the incident energy (Figure 31). All the fluorescence emission lines derived from TRXF scan were fitted with Gaussian line shapes (Figure 32).
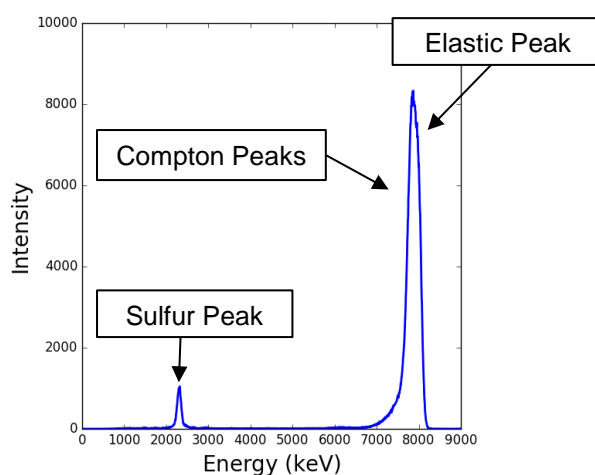

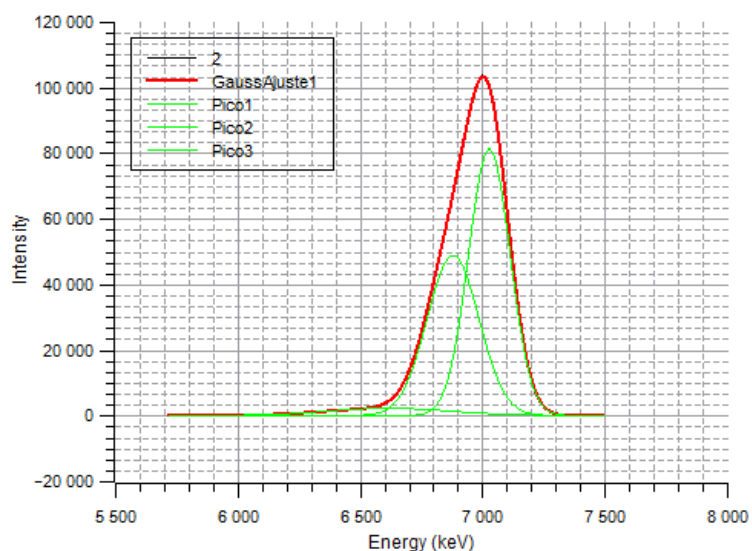Figure 31 – Sulfur, Compton and Elastic Peak. Incident energy : 8keV.

Figure 32 – Compton peaks and Rayleigh peak fitted with Gaussian line shape. Incident energy : 7 keV.

As said before, the TRXF experiment lasted two days, in which: on the first day, it was performed a first compression (Figure 33) and decompression; and on the second day, a recompression followed by a decompression. This experiment aimed to follow the evolution of the sulfur content during each compression/ decompression cycle (Figure 34).
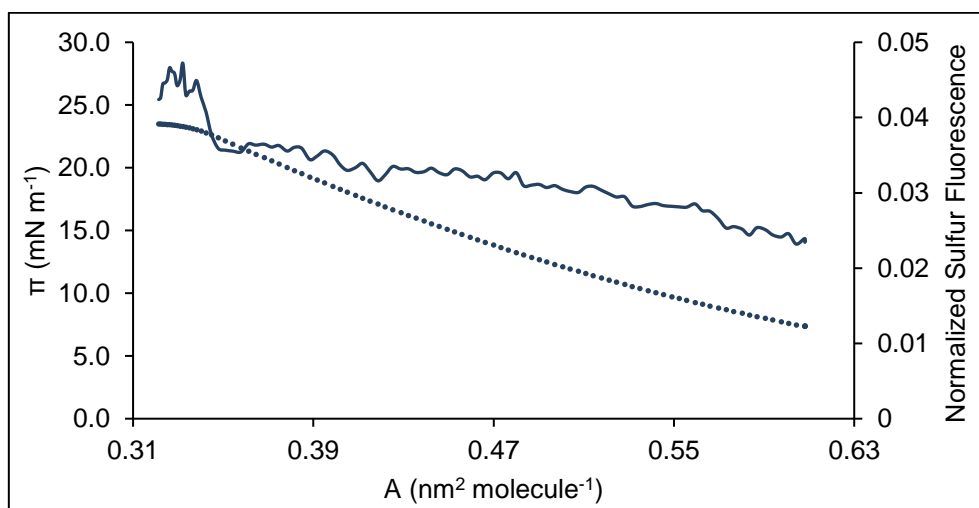

Figure 33 – Normalized Sulfur Fluorescence (**plain curve**) along the first compression and correspondent surface pressure (**dotted curve**).
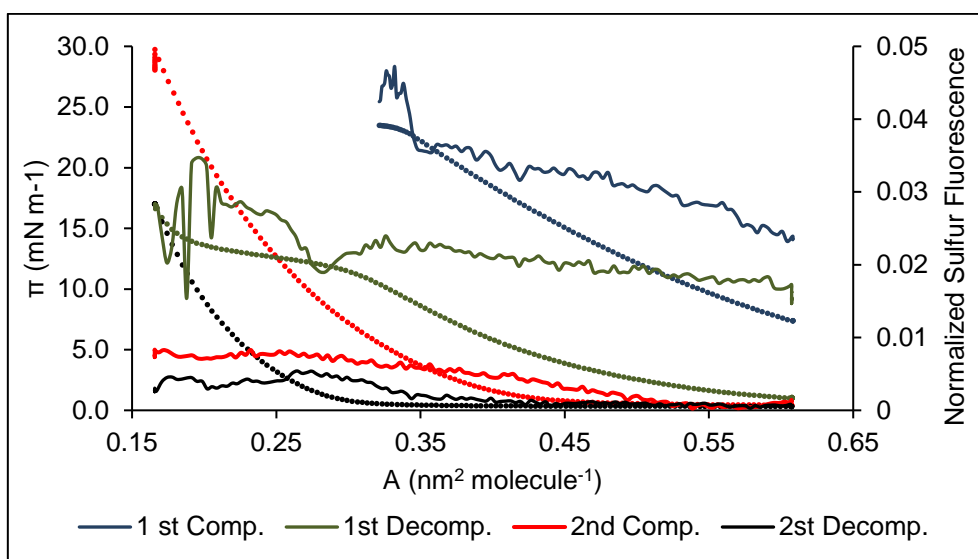
Figure 34 – Normalized Sulfur Fluorescence (**plain curve**) along two compression/ decompression cycles and correspondent surface pressure (**dotted curve**).

From the results, it is observed that during the first compression, the sulfur fluorescence level is gradually rising due to the increase in surface density, until the plateau is reached. At this moment, the surface pressure does not evolve, but there is a step increase of the sulfur fluorescence intensity. This happens due to crystal formation on the interface. This is in agreement with the appearance of crystalline-like structures on BAM images and peaks in GIXD. It is possible to say that crystal formation on the surface happens at this point.

At the beginning of decompression, it is first observed some perturbation on sulfur fluorescence. Then, at the end of the plateau, a big decrease of the fluorescence, followed by a small increase and gradual decrease until end of expansion. The big decrease of the fluorescence happens at the end of the plateau, that occurs at a surface pressure similar to the ESP value, meaning that at this point the crystalline-like structures disappear. The gradual decrease of sulfur fluorescence happens with the decrease of the crystals on the surface.

After one day, the monolayer was recompressed and decompressed. In this second compression/ decompression cycle, it is observed a small increase of sulfur fluorescence, smaller than the compression/ decompression performed in the first day (fluorescence maximum difference in the compressions: 0.035; fluorescence maximum difference in the decompressions: 0.025).

Therefore, the sulfur fluorescence level decreases with the compressions and decompressions. This means that the quantity of [NTf$_2$] anions at the surface are decreasing, so they are disappearing from the surface. This disappearing could happen due to dissolution of the anion in the subphase, however the existence of an equilibrium isotherm contradicts its complete dissolution. However, (π-A)

measurement and TRXF are not sensitive to the same element. The (π-A) isotherms are mainly determined by the long chain cations; whereas, TRXF measures only the presence of [NTf$_2$] anion at the interface. Thus, it can be concluded that long chain cations remain at the interface and the anions dissolves in the subphase.

IV. Conclusion and future remarks

Results from Langmuir Isotherms, on both subphases, pure and salt water, showed clearly that [C$_{18}$mim][NTf$_2$] is more stable comparing to others from its family, [C$_n$mim][NTf$_2$] (n=12,14 and 16), and to [C$_{18}$mim][Cl] and [C$_{18}$mim][PF$_6$]. It was also proved that the addition of NaCl stabilizes the monolayer.

From the first compression/ decompression behaviour, it can be concluded that the first compression induces reversible formation of crystals above the ESP value:

- (π-A) isotherms show a gradual increase in surface pressure up to 0.27 nm^2 molecule^{-1}, where then a plateau region appears (0.27-0.17 nm^2 molecule^{-1}), a highly compressible region, probably due the appearance of crystals at the surface;
- by the appearance of bright spots and a thicker film, BAM results suggest the existence of a monolayer in coexistence with multi-layered structures. Results showed that: on pure water, crystalline-like sctructures exists; and on salt water, the existence of dense agglomerates is verified, however crystalline areas were not observed, not making possible its confirmation;
- on GIXD experiments, it was obtained peaks above the ESP value and with the help of XRD, it can be concluded that diffraction comes from 3D crystals/ multilayer formed at the air/ pure water interface;
- on TRXF results, the step increase of sulfur fluorescence intensity, when the plateau is reached is also in agreement with the appearance of crystalline-like structures.

In the long term behaviour, an evolution of the layer is observed:

- the (π-A) isotherms shift to smaller molecular areas and smaller surface pressures, which suggests an evolution in the layer leading to a loss in area, attributed to a loss of molecules by dissolution on the subphase at the first sight. Although an equilibrium isotherm exists meaning that the dissolution is not complete;
- BAM results show a disappearance of the domains when the film is further compressed;
- the TRXF results of [C$_{18}$mim][NTf$_2$] suggest that the anions are disappearing from the interface by dissolution in water;
- this evolution can be due to a conformational change of the IL on water where anions are disappearing, leaving at the interface only long chain cation.

In future works, it would be interesting to perform BAM experiments on the same conditions used in the present work in order to obtain better images and to complement the present results. It would be also interesting to analyse [C$_{18}$mim][NTf$_2$] when further compressed by experiments such as (π-A) Langmuir isotherms, BAM and X-ray experiments. This study could help to understand what happens to the monolayer. Besides the analysis of further compression, the study of the molecule for different relaxation times would be also interesting as well as to study the behaviour at the interface of ILs with longer chains ([C$_{20}$mim]$^+$, [C$_{22}$mim]$^+$,…), for which dissolution is highly unlikely.

V. References

Accurion-Solutions for Science. (2014). Brewster Angle Microscopy | Accurion. Retrieved July 14, 2016, from http://www.accurion.com/brewster-angle-microscopy

Aldrich. (2005). ChemFiles: Enabling Technologies, *5*(6). Retrieved from https://www.sigmaaldrich.com/content/dam/sigma-aldrich/docs/Aldrich/Brochure/al_chemfile_v5_n6.pdf

Bai, X., Li, X., & Zheng, L. (2010). Chiral Ionic Liquid Monolayer-Stabilized Gold Nanoparticles: Synthesis, Self-Assembly, and Application to SERS. *Langmuir*, *26*(14), 12209–12214.

Beckhoff, B., Kanngießer, habil. B., Langhoff, N., Wedell, R., & Wolff, H. (2006). *Handbook of Practical X-Ray Fluorescence Analysis*. Berlin, Heidelberg: Springer Berlin Heidelberg.

Benz, N. (2015). A Lego® Brewster Angle Microscope for Quantitative Monolayer Film Analysis., Department of Chemistry, California Polytechnic State University, San Luis Obispo, California. Retrieved from http://digitalcommons.calpoly.edu/physsp/

Dutta, P. (2000). Grazing incidence X-ray diffraction. *Current Science*, *78*(12), 1478–1483.

Filipe, E. J. M., Morgado, P., Teixeira, M., Shimizu, K., Bonatout, N., Goldmann, M., & Canongia, J. N. L. (2016). Crystalline-like structures and multilayering in Langmuir films of ionic liquids at the air–water interface. *Chem. Commun.*, *52*(32), 5585–5588.

Fontaine, P., Ciatto, G., Aubert, N., & Goldmann, M. (2014). Soft Interfaces and Resonant Investigation on Undulator Source: A Surface X-ray Scattering Beamline to Study Organic Molecular Films at the SOLEIL Synchrotron. *Science of Advanced Materials*, *6*(11), 2312–2316.

Gaines, G. L. (1966). *Insoluble monolayers at liquid-gas interfaces*. New York: John Wiley& Sons, Inc.

Gamboa, A. L. (2006). *Ordering in Langmuir and Langmuir-Blodgett Films: effect of the presence of fluorocarbon and hydrocarbon chains*. Instituto Superior Técnico, Lisboa.

Görgl, R., Wobrauschek, P., Kregsamer, P., Streli, C., Haller, M., Knöchel, A., & Radtke, M. (1997). Total Reflection X-Ray Fluorescence Analysis Excited by Synchrotron Radiation (SR-TXRF): Variation of Excitation Conditions and Sample Geometries. *X-Ray Spectrometry*, *26*(4), 189–194. John Wiley & Sons, Ltd.

Haschke, M. (2014). XRF-Basics. In *Laboratory Micro-X-Ray Fluorescence Spectroscopy* (pp. 1–17).

Hayes, R., Warr, G. G., & Atkin, R. (2015). Structure and Nanostructure in Ionic Liquids. *Chemical Reviews*, *115*(13), 6357–6426.

Hénon, S., & Meunier, J. (1991). Microscope at the Brewster angle: Direct observation of first-order

phase transitions in monolayers. *Review of Scientific Instruments*, *62*(4), 936–940.

Hoenig, D., & Moebius, D. (1991). Direct visualization of monolayers at the air-water interface by Brewster angle microscopy. *The Journal of Physical Chemistry*, *95*(12), 4590–4592.

Jia, H., Bai, X., Zheng, L., Cobley, C. M., Chen, J. E., Cho, C. L., … Nogami, M. (2012). One-step synthesis and assembly of gold nanochains using the Langmuir monolayer of long-chain ionic liquids and their applications to SERS. *CrystEngComm*, *14*(8), 2920–2925.

Kuboki, T., Okuyama, T., Ohsaki, T., & Takami, N. (2005). Lithium-air batteries using hydrophobic room temperature ionic liquid electrolyte. *Journal of Power Sources*, *146*(1–2), 766–769.

KYOWA Leading Answers. (2014). What is Surface Tension? :Kyowa Interface Science. Retrieved July 20, 2016, from http://www.face-kyowa.co.jp/english/en_science/en_theory/en_what_Surface_tension/

Larsen, M. C. (2014). Binary Phase Diagrams at the Air–Water Interface: An Experiment for Undergraduate Physical Chemistry Students. *Journal of Chemical Education*, *91*(4), 597–601.

Lewandowski, A., & Świderska-Mocek, A. (2009). Ionic liquids as electrolytes for Li-ion batteries—An overview of electrochemical studies. *Journal of Power Sources*, *194*(2), 601–609.

Marra, W. C., Eisenberger, P., & Cho, A. Y. (1979). X-ray total-external-reflection–Bragg diffraction: A structural study of the GaAs-Al interface. *Journal of Applied Physics*, *50*(11), 6927–6934.

Mobilio, S., & Balerma, A. (2003). Introduction to Synchrotron Radiation. *Synchrotron Radiation: Basics, Methods and Applications*, 1–23. Italy, Springer.

Mukherjee, I., Mukherjee, S., Naskar, B., Ghosh, S., & Moulik, S. P. (2013). Amphiphilic behavior of two phosphonium based ionic liquids. *Journal of Colloid and Interface Science*, *395*, 135–144.

Park, B. J., Pantina, J. P., Furst, E. M., Oettel, M., And, S. R., & Vermant, J. (2008). Direct Measurements of the Effects of Salt and Surfactant on Interaction Forces between Colloidal Particles at Water−Oil Interfaces. *Langmuir*, *24*(5), 1686–1694.

Pecharsky, V. K., & Zavalij, P. Y. (2009). *Fundamentals of powder diffraction and structural characterization of materials.* U.S.A.: Springer.

Plechkova, N. V., Seddon, K. R., Chauvin, Y., Hückel, W., Walden, P., Tokuda, H., & Tsuzuki, S. (2008). Applications of ionic liquids in the chemical industry. *Chem. Soc. Rev.*, *37*(1), 123–150.

Rogers, R. D., & Seddon, K. R. (2003). Ionic Liquids--Solvents of the Future? *Science*, *302*(5646), 792–793.

Sloutskin, E., Ocko, B. M., Tamam, L., Kuzmenko, I., Gog, T., & Deutsch, M. (2005). Surface Layering in Ionic Liquids: An X-ray Reflectivity Study. *Journal of the American Chemical Society*, 7796–

7804.

SOLEIL Synchrotron. (2016). SIRIUS. Retrieved July 30, 2016, from httpp://www.synchrotron-soleil.fr/Recherche/LignesLumiere/SIRIUS

Tamam, L., Ocko, B. M., Reichert, H., & Deutsch, M. (2011). Checkerboard Self-Patterning of an Ionic Liquid Film on Mercury. *Physical Review Letters*, *106*(19), 197801.

Tavares, A. P., Rodriguez, O., & Macedo, E. A. (2013). New Generations of Ionic Liquids Applied to Enzymatic Biocatalysis. In *Ionic Liquids - New Aspects for the Future* (pp. 539–556). InTech.

Wasserscheid, P., & Welton, T. (Eds.). (2002). *Ionic Liquids in Synthesis.* Weinheim, FRG.

Welton, T. (1999). Room-Temperature Ionic Liquids. Solvents for Synthesis and Catalysis. *Chemical Reviews*, *99*(8), 2071–2084.

WikimediaFoundation. (2016). Retrieved July 25, 2016.

Wobrauschek, P. (2007). Total reflection x-ray fluorescence analysis—a review. *X-Ray Spectrometry*, *36*(5), 289–300. John Wiley & Sons, Ltd.

Wu, H., Chen, M., Fan, Y., Elsebaei, F., & Zhu, Y. (2012). Determination of rutin and quercetin in Chinese herbal medicine by ionic liquid-based pressurized liquid extraction–liquid chromatography–chemiluminescence detection. *Talanta*, *88*, 222–229.

Zhao, L., Hu, Y.-S., Li, H., Wang, Z., & Chen, L. (2011). Porous Li4Ti5O12 Coated with N-Doped Carbon from Ionic Liquids for Li-Ion Batteries. *Advanced Materials*, *23*(11), 1385–1388.

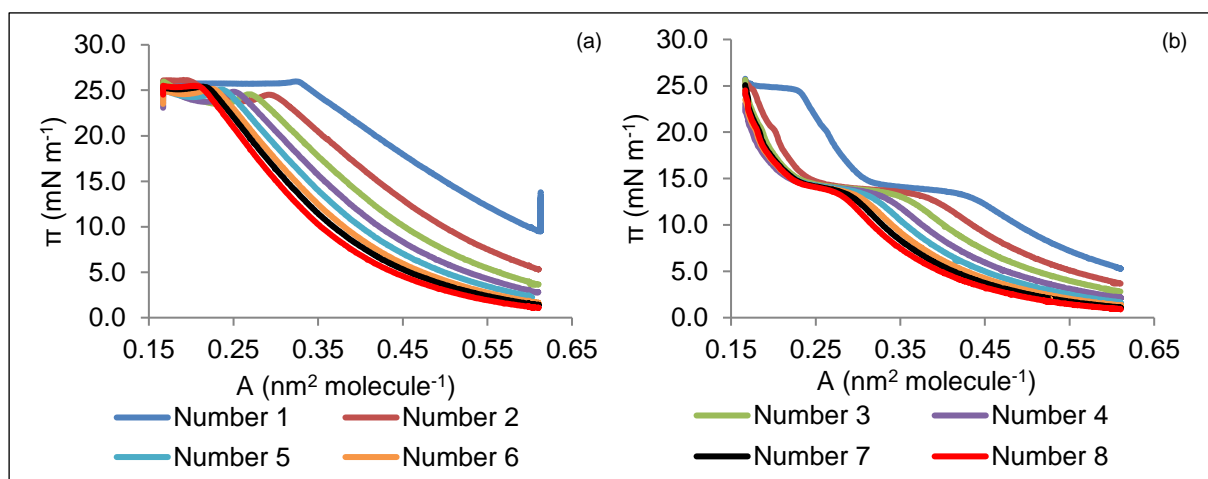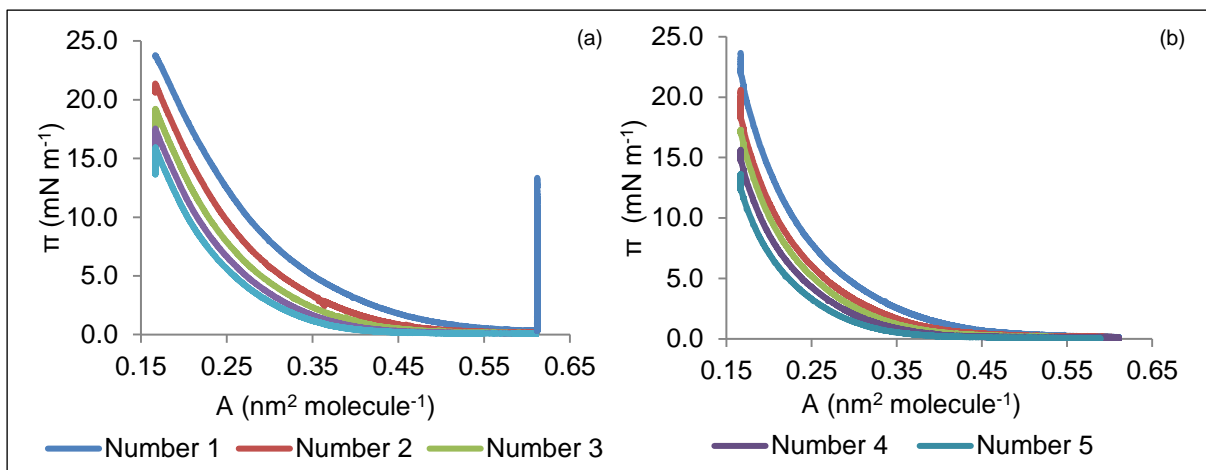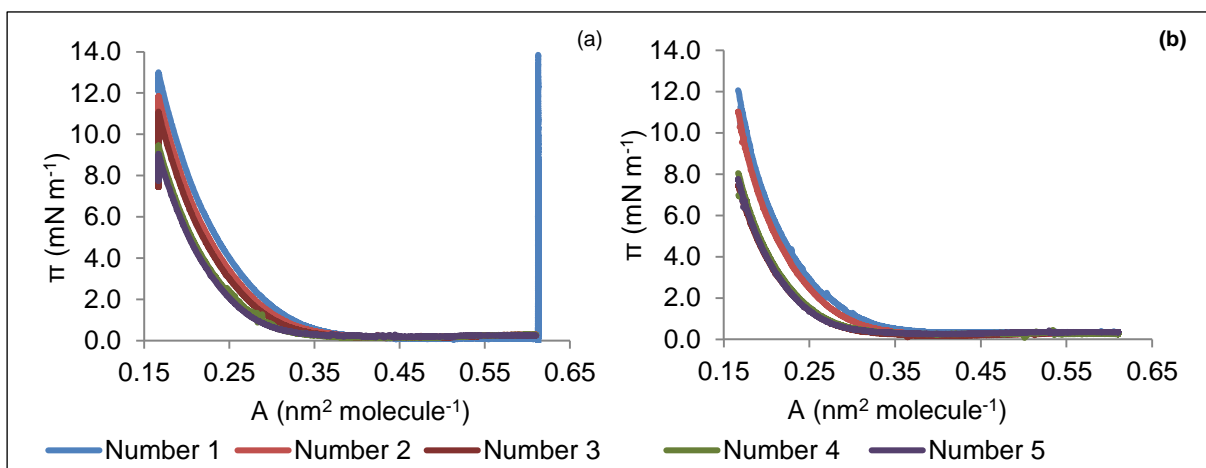# VI. Appendix

VI.1. Langmuir Isotherms
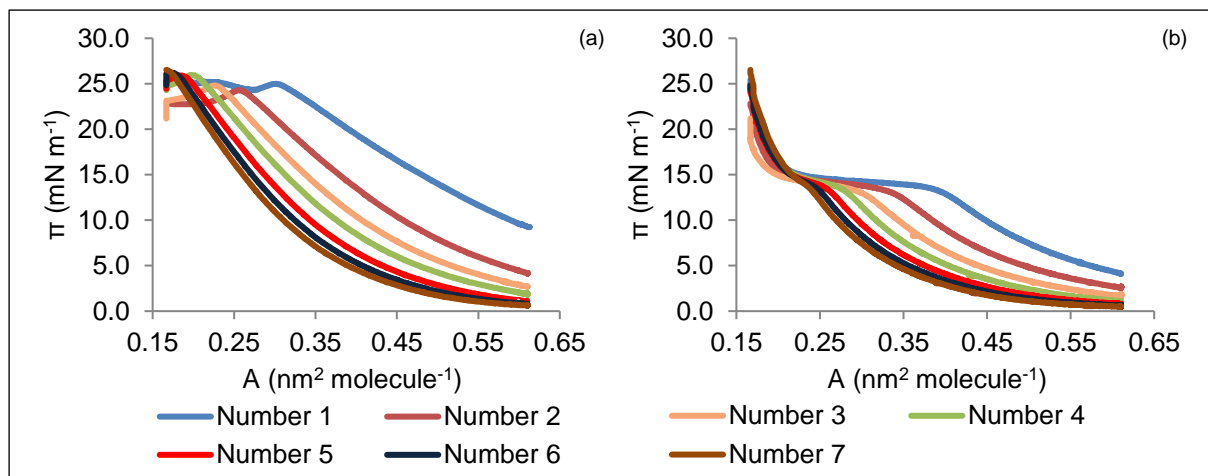
Figure A 1 – ISOT18120 – Seven compression/ decompression cycles with [C_{18}mim][NTf_2]: (a) Compressions; and (b) Decompressions made. Isotherm performed at air/ pure water interface, after 10 minutes of solvent evaporation at a compression rate of 36 cm^2 min^{-1} (0.0004 nm^2 sec^{-1} $molecule^{-1}$).
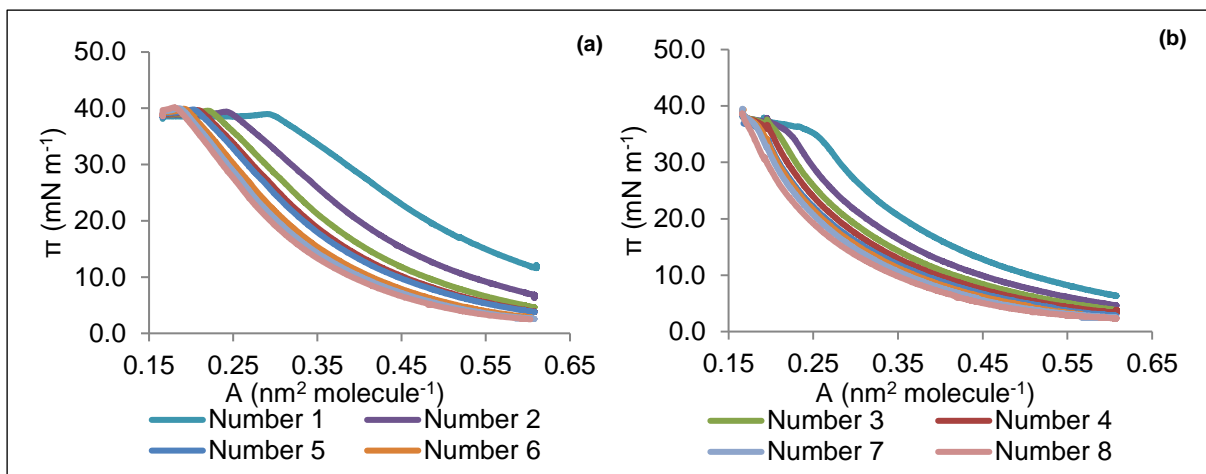

Figure A 2 – ISOT18240 – Eight compression/ decompression cycles with [C_{18}mim][NTf_2]: (a) Compressions; and (b) Decompressions made. Isotherm performed at air/ pure water interface, after 10 minutes of solvent evaporation at a compression rate of 69 cm^2 min^{-1} (0.0008 nm^2 sec^{-1} $molecule^{-1}$).
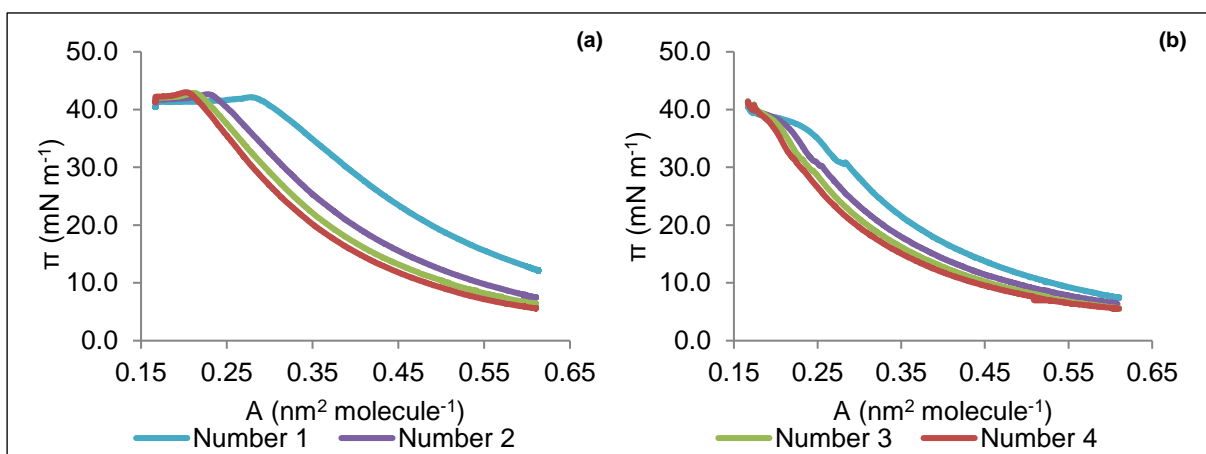
Figure A 3 – ISOT18N – Five compression/ decompression cycles with [C_{18}mim][NTf$_2$]: (a) Compressions; and (b) Decompressions made. Isotherm performed at air/ pure water interface, after one N of solvent evaporation at a compression rate of 20 cm^2 min^{-1} (0.0002 nm^2 sec^{-1} molecule^{-1}).
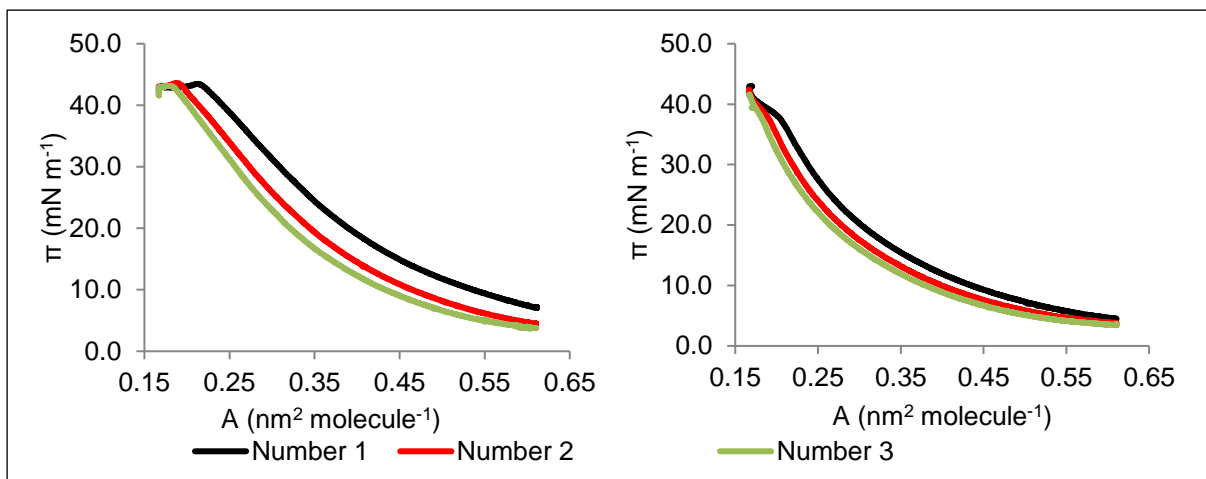

Figure A 4 – ISOT18WE – Five compression/ decompression cycles with [C_{18}mim][NTf$_2$]: (a) Compressions; and (b) Decompressions made. Isotherm performed at air/ pure water interface, after one WE of solvent evaporation at a compression rate of 20 cm^2 min^{-1} (0.0002 nm^2 sec^{-1} molecule^{-1}).

Figure A 5 – ISOTS18120 – Eight compression/ decompression cycles with [C$_{18}$mim][NTf$_2$]: (a) Compressions; and (b) Decompressions made. Isotherm performed at air/ salt water interface, after 10 minutes of solvent evaporation at a compression rate of 36 cm^2 min^{-1} (0.0004 nm^2 sec^{-1} molecule^{-1}).
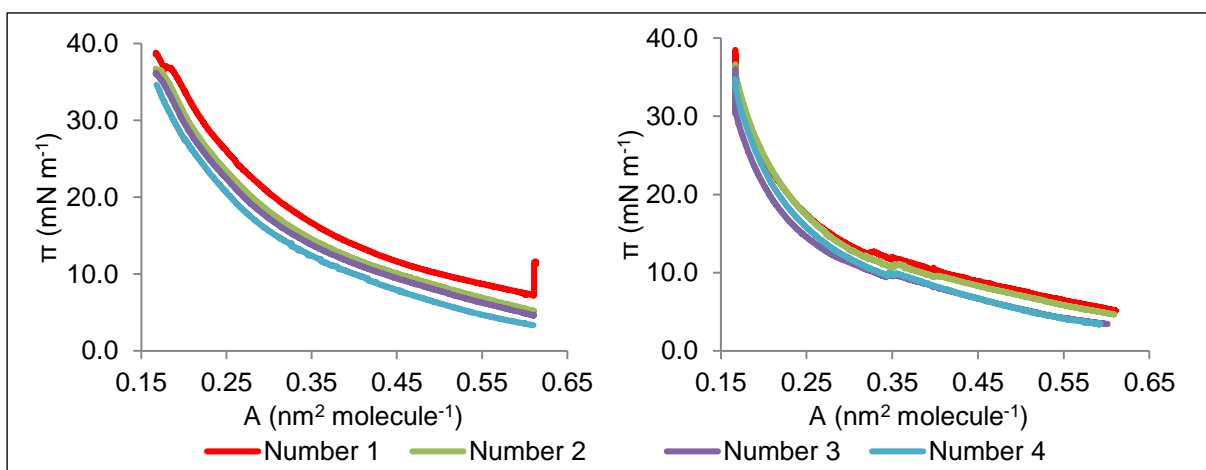

Figure A 6 – ISOTS18240 – Four compression/ decompression cycles with [C$_{18}$mim][NTf$_2$]: (a) Compressions; and (b) Decompressions made. Isotherm performed at air/ salt water interface, after 10 minutes of solvent evaporation at a compression rate of 69 cm^2 min^{-1} (0.0008 nm^2 sec^{-1} molecule^{-1}).

Figure A 7 – ISOTS18N -– Three compression/ decompression cycles with [C_{18}mim][NTf_2]: (a) Compressions; and (b) Decompressions made. Isotherm performed at air/ salt water interface, after one N of solvent evaporation at a compression rate of 20 cm^2 min^{-1} (0.0002 nm^2 sec^{-1} molecule^{-1}).

Figure A 8 – ISOTS18WE – Four compression/ decompression cycles with [C_{18}mim][NTf_2]: (a) Compressions; and (b) Decompressions made. Isotherm performed at air/ salt water interface, after one WE of solvent evaporation at a compression rate of 20 cm^2 min^{-1} (0.0002 nm^2 sec^{-1} molecule^{-1}).
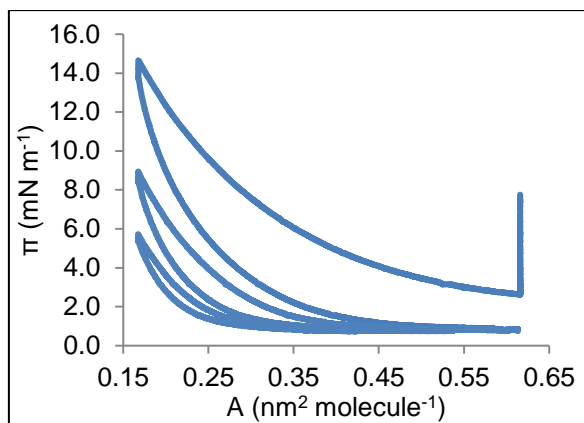
Figure A 9 – ISOT1660 – Three compression/ decompression cycles with [C_{16}mim][NTf$_2$]. Isotherm performed at air/ pure water interface, after 10 minutes of solvent evaporation at a compression rate of 20 cm^2 min^{-1} (0.0002 nm^2 sec^{-1} molecule^{-1}).
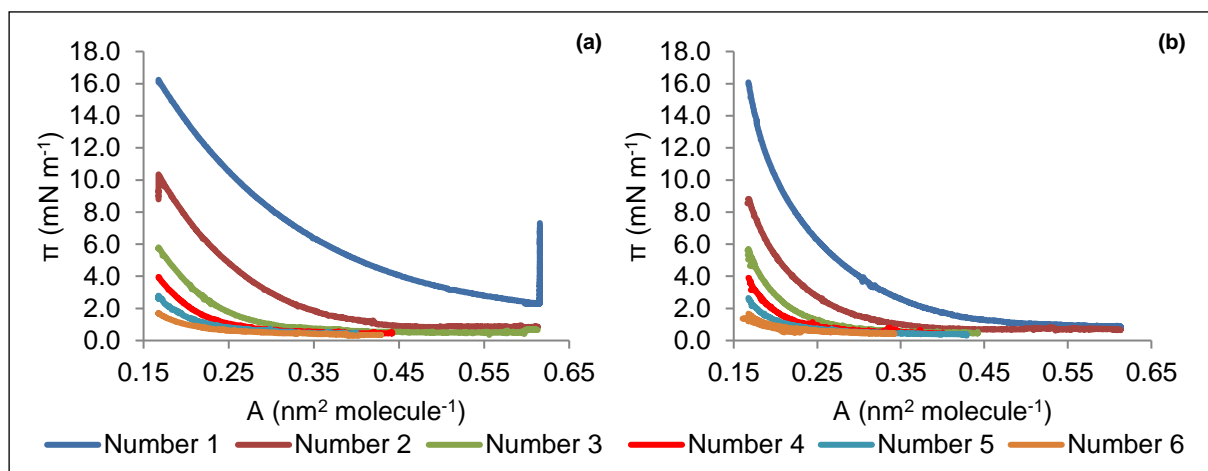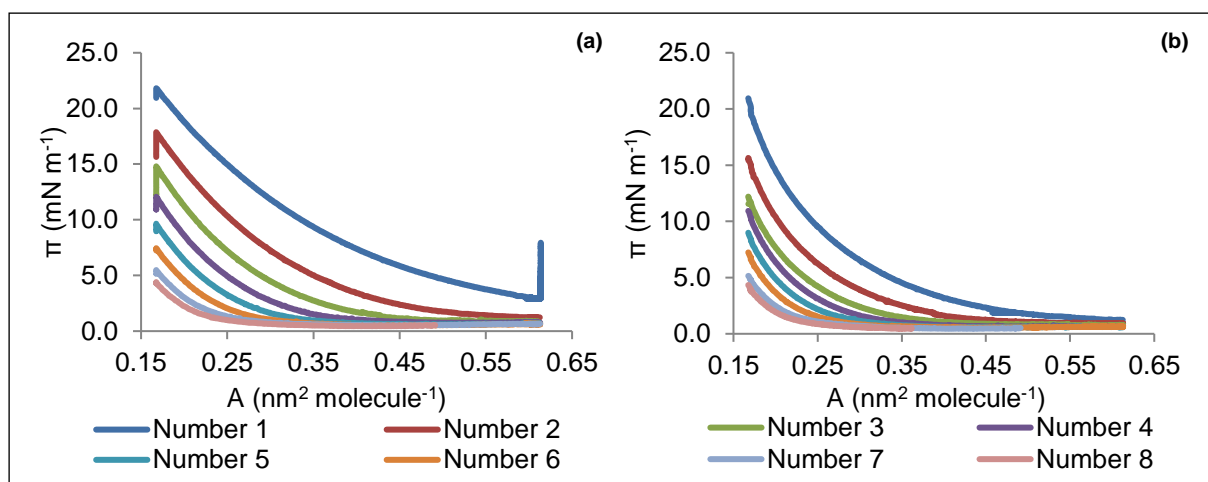

Figure A 10 – ISOT16120 – Six compression/ decompression cycles with [C_{16}mim][NTf$_2$]: (a) Compressions; and (b) Decompressions made. Isotherm performed at air/ pure water interface, after 10 minutes of solvent evaporation at a compression rate of 36 cm^2 min^{-1} (0.0004 nm^2 sec^{-1} molecule^{-1}).

Figure A 11 – ISOT16240 – Eight compression/ decompression cycles with [C$_{16}$mim][NTf$_2$]: (a) Compressions; and (b) Decompressions made. Isotherm performed at air/ pure water interface, after 10 minutes of solvent evaporation at a compression rate of 69 cm^2 min^{-1} (0.0008 nm^2 sec^{-1} molecule^{-1}).
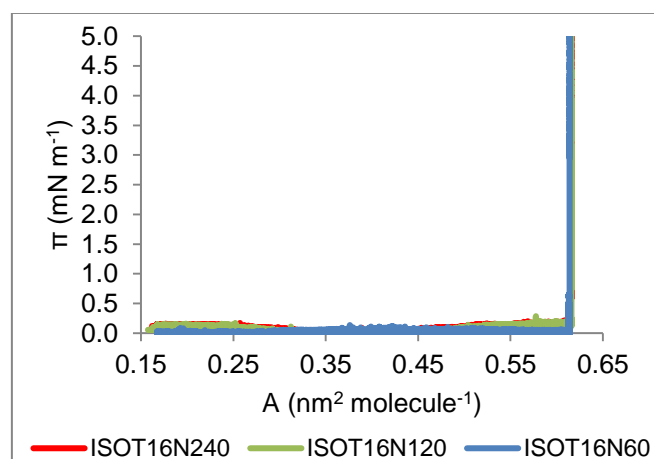

Figure A 12 – One compression/ decompression cycle made with [C$_{16}$mim][NTf$_2$] at a compression rate of 20 (ISOT16N60; **blue line**), 36 (ISOT16N120; **green line**) and 69 cm^2 min^{-1} (ISOT16N240; **red line**). Isotherm performed at air/ pure water interface, after one N of solvent evaporation.
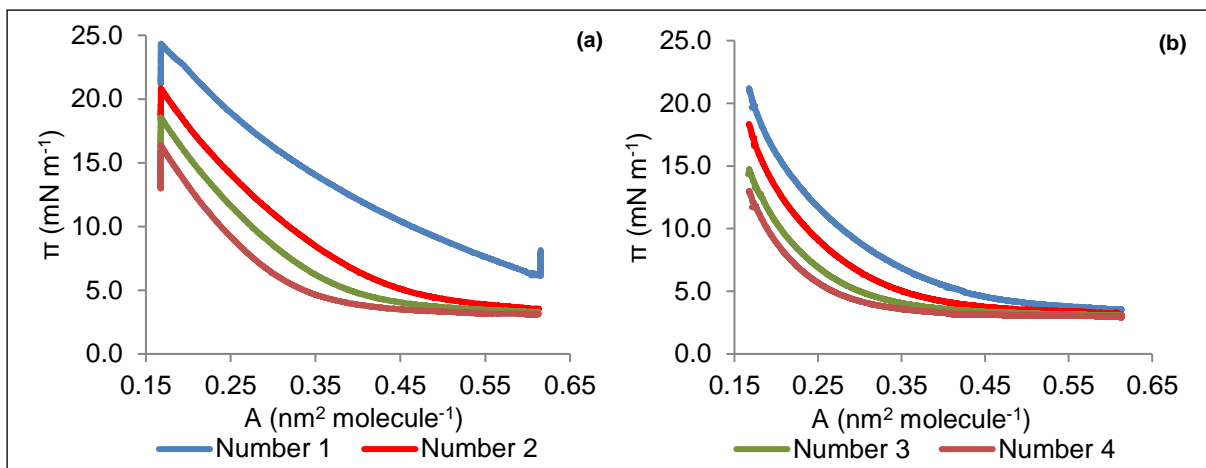
Figure A 13 – ISOTS1660 – Four compression/ decompression cycles with [C$_{16}$mim][NTf$_2$]: (a) Compressions; and (b) Decompressions made. Isotherm performed at air/ salt water interface, after 10 minutes of solvent evaporation at a compression rate of 20 cm^2 min^{-1} (0.0002 nm^2 sec^{-1} molecule^{-1}).
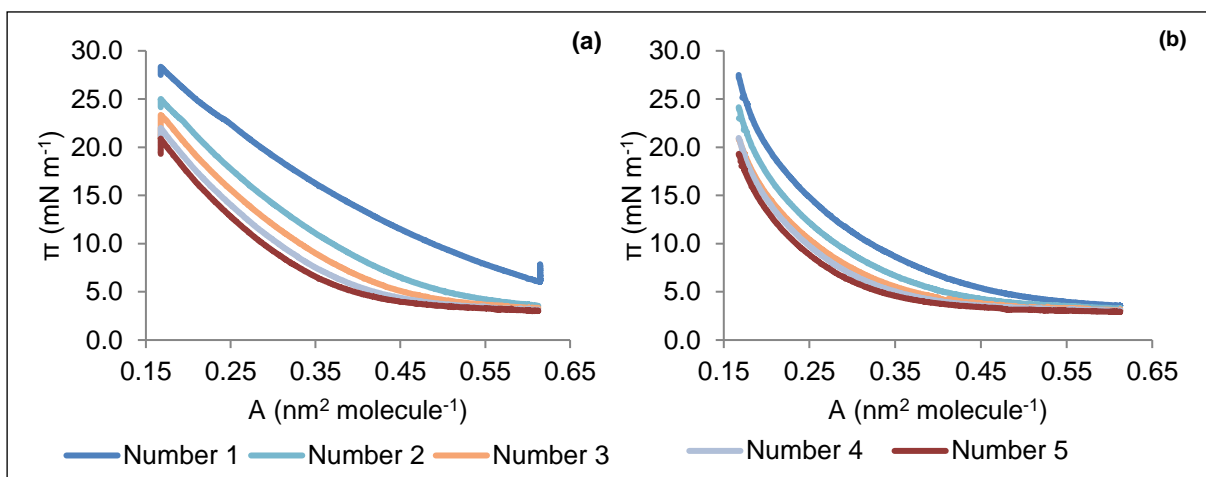

Figure A 14 – ISOTS16120 – Five compression/ decompression cycles with [C$_{16}$mim][NTf$_2$]: (a) Compressions; and (b) Decompressions made. Isotherm performed at air/ salt water interface, after 10 minutes of solvent evaporation at a compression rate of 36 cm^2 min^{-1} (0.000a nm^2 sec^{-1} molecule^{-1}).
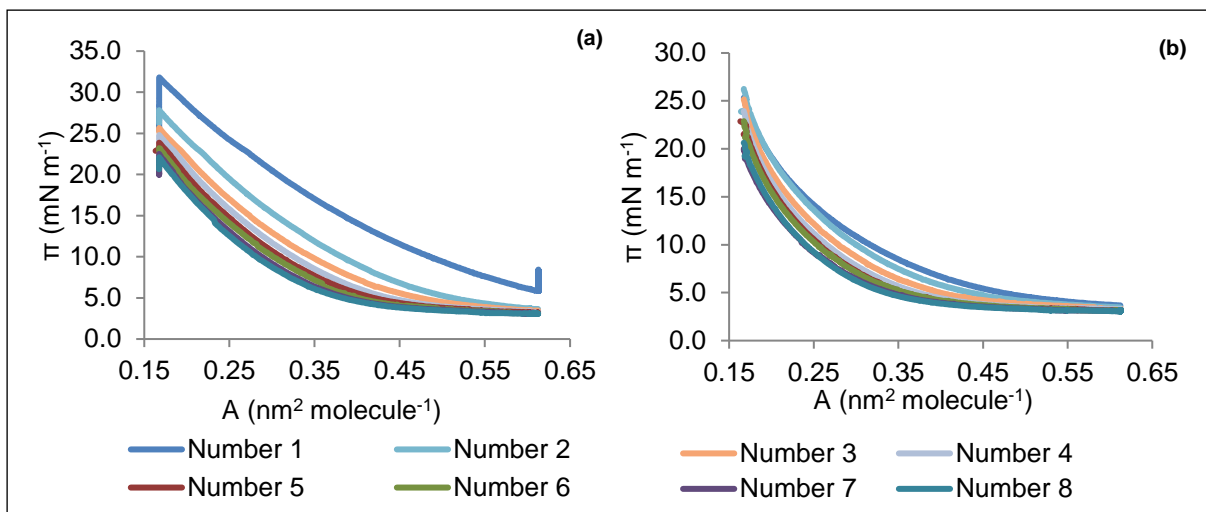
Figure A 15 - ISOTS16240 – Eight compression/ decompression cycles with [C$_{16}$mim][NTf$_2$]: (a) Compressions; and (b) Decompressions made. Isotherm performed at air/ salt water interface, after 10 minutes of solvent evaporation at a compression rate of 69 cm^2 min^{-1} (0.0008 nm^2 sec^{-1} molecule^{-1}).
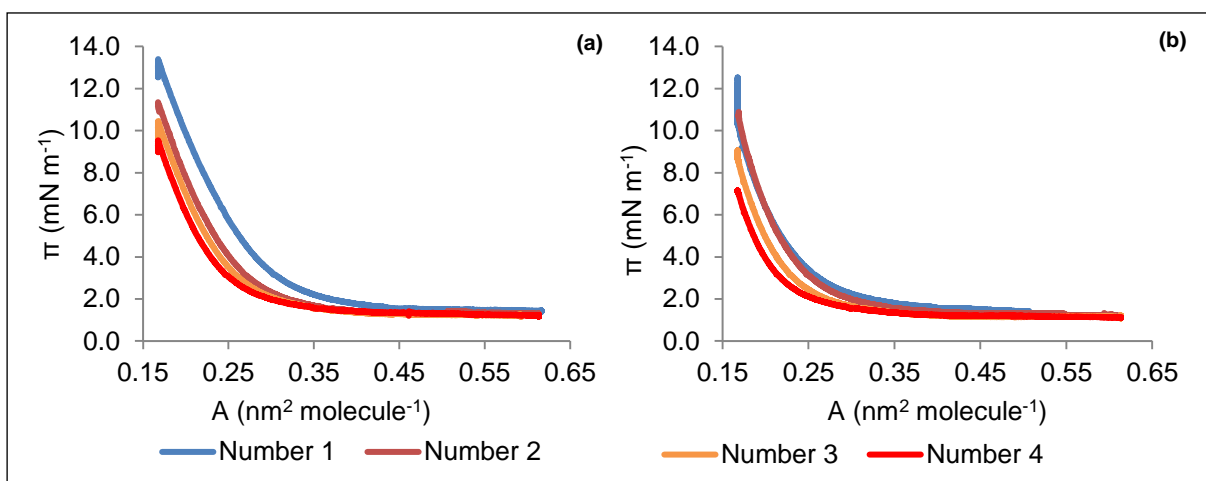

Figure A 16 – ISOTS16N – Four compression/ decompression cycles with [C$_{16}$mim][NTf$_2$]: (a) Compressions; and (b) Decompressions made. Isotherm performed at air/ pure water interface, after one N of solvent evaporation at a compression rate of 20 cm^2 min^{-1} (0.0002 nm^2 sec^{-1} molecule^{-1}).
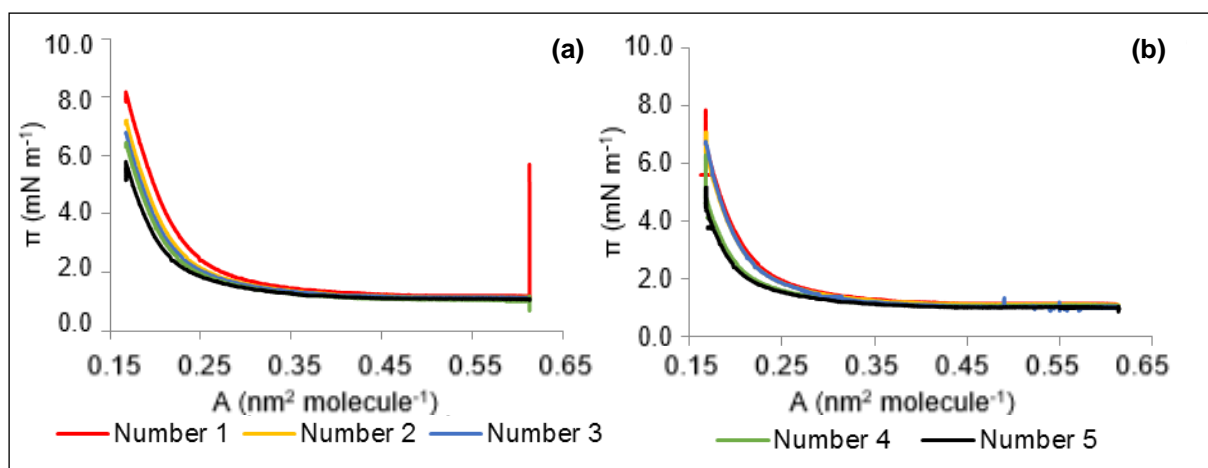
Figure A 17 – ISOTS16WE – Five compression/ decompression cycles with [C$_{16}$mim][NTf$_2$]: (a) Compressions; and (b) Decompressions made. Isotherm performed at air/ pure water interface, after one WE of solvent evaporation at a compression rate of 20 cm^2 min^{-1} (0.0002 nm^2 sec^{-1} molecule^{-1}).

Figure A 18 – ISOT1460 – One compression/ decompression cycles with [C$_{14}$mim][NTf$_2$]. Isotherm performed at air/ pure water interface, after 10 minutes of solvent evaporation at a compression rate of 20 cm^2 min^{-1} (0.0002 nm^2 sec^{-1} molecule^{-1}).
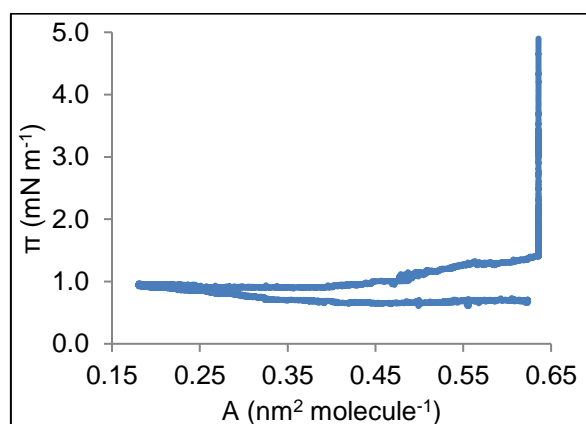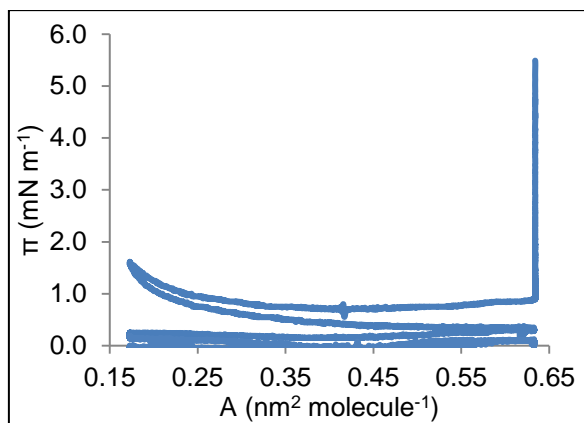
Figure A 19 – ISOT14120 – Two compression/ decompression cycles with [C$_{14}$mim][NTf$_2$]. Isotherm performed at air/ pure water interface, after 10 minutes of solvent evaporation at a compression rate of 36 cm^2 min^{-1} (0.0004 nm^2 sec^{-1} molecule^{-1}).
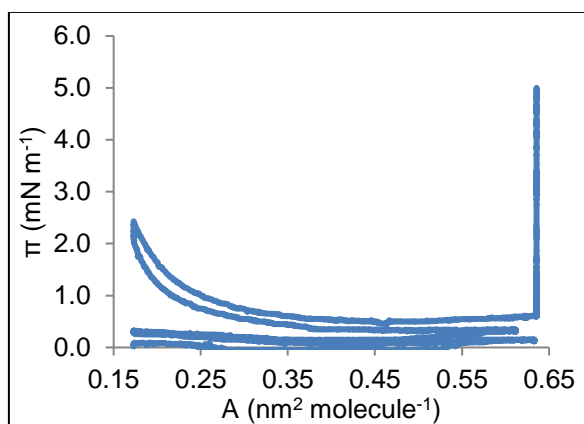

Figure A 20 – ISOT14240 – Three compression/ decompression cycles with [C$_{14}$mim][NTf$_2$]. Isotherm performed at air/ pure water interface, after 10 minutes of solvent evaporation at a compression rate of 69 cm^2 min^{-1} (0.0008 nm^2 sec^{-1} molecule^{-1}).
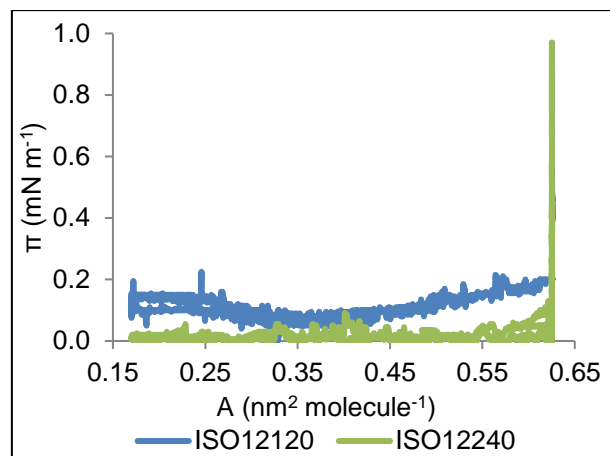
Figure A 21 – ISOT12120 and ISOT12240 – One compression/ decompression cycle with the molecule [C_{12}mim][NTf$_2$]. Isotherms performed at air/ pure water interface, after 10 minutes of solvent evaporation at a compression rate of 36 cm^2 min^{-1} (**blue line**) and at a compression rate of 69 cm^2 min^{-1} (**green line**).
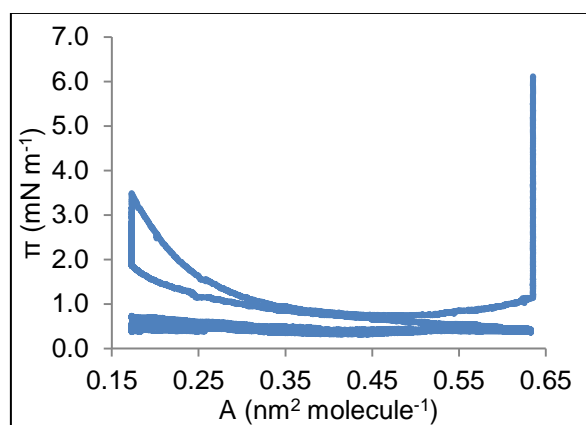
Figure A 22 – ISOTS1460 – Three compression/ decompression cycles with [C_{14}mim][NTf$_2$]. Isotherm performed at air/ salt water interface, after 10 minutes of solvent evaporation at a compression rate of 20 cm^2 min^{-1}.

Figure A 23 – ISOTS14120 – Four compression/ decompression cycles with [C_{14}mim][NTf_2]: (a) Compressions; and (b) Decompressions made. Isotherm performed at air/ salt water interface, after 10 minutes of solvent evaporation at a compression rate of 36 cm^2 min^{-1}.

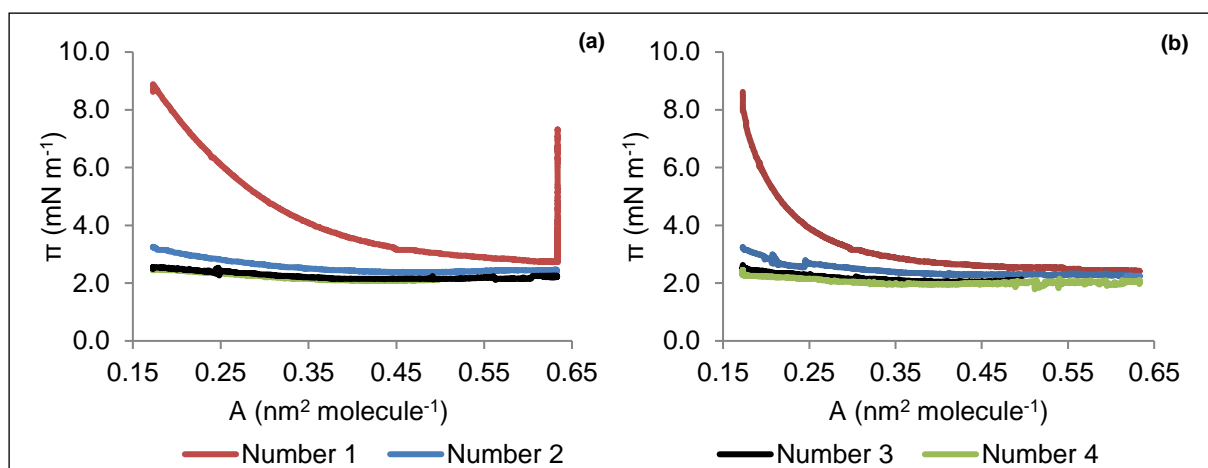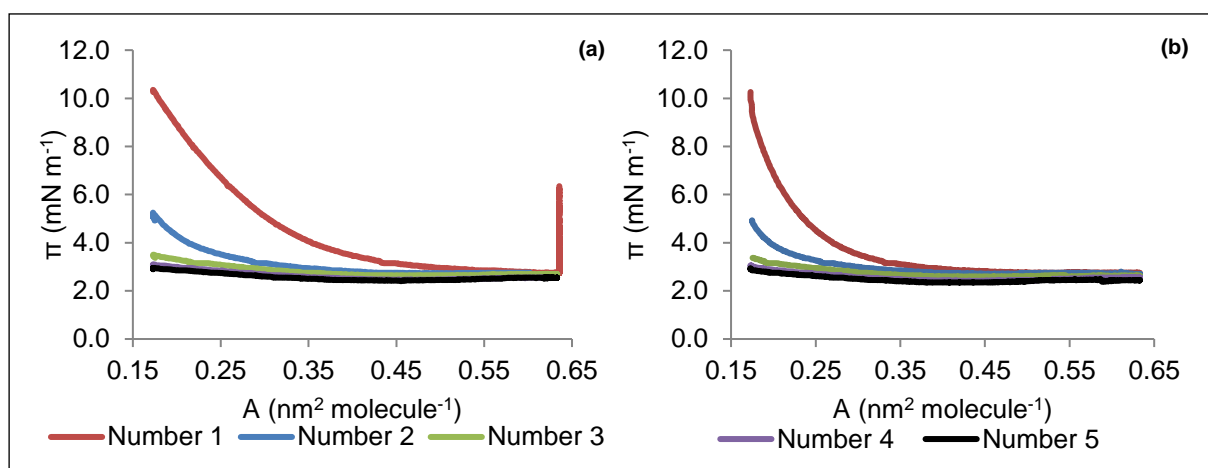Figure A 24 – ISOTS14240 – Five compression/ decompression cycles with [C_{14}mim][NTf_2]: (a) Compressions; and (b) Decompressions made. Isotherm performed at air/ salt water interface, after 10 minutes of solvent evaporation at a compression rate of 69 cm^2 min^{-1}.
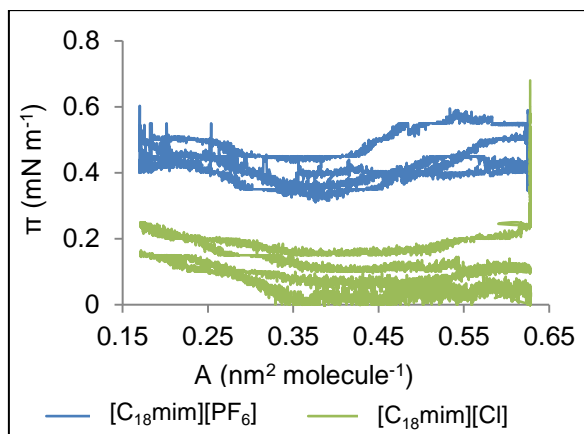
Figure A 25 – Two compression/ decompression cycles made with [C_{18}mim][Cl] (**green line**) and [C_{18}mim][PF_6] (**blue line**). Isotherm performed at air/ pure water interface, after 10 minutes of solvent evaporation at a compression rate of 20 cm^2 min^{-1}.

VI.2. Equilibrium Isotherm
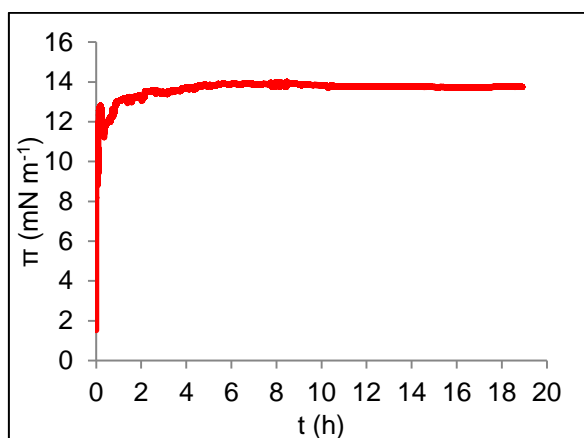
Figure A 26 – Example of π vs time curve to obtain ESP value of [C_{18}mim][NTf_2] at air/ pure water interface. ESP value obtained: 13.8 mN m^{-1}.

VI.3. Equilibrium Spreading Pressure (ESP)

Table A 1 – Values of equilibrium area per molecule, A_0, for each fixed surface area, π, for ISOT1860.

Isotherm	ISOT1860			
π (mN m^{-1})	5.0	10.0	15.0	20.0
A_0 (nm^2 $molecule^{-1}$)	0.25±0.04	0.25±0.01	0.20±0.01	0.17±0.01
R^2	0.9929	0.9881	0.9884	0.9941

Table A 2 – Values of equilibrium area per molecule, A_0, for each fixed surface area, π, ISOT18120.

Isotherm	ISOT18120				
π (mN m^{-1})	5.0	10.0	15.0	20.0	24.0
A_0 (nm^2 molecule^{-1})	0.26±0.08	0.30±0.02	0.25±0.01	0.21±0.01	0.18±0.01
R^2	0.9876	0.9788	0.9798	0.9790	0.9778

Table A 3 – Values of equilibrium area per molecule, A_0, for each fixed surface area, π, for ISOT18240.

Isotherm	ISOT18240				
π (mN m^{-1})	6.0	10.0	15.0	20.0	24.0
A_0 (nm^2 molecule^{-1})	0.37±0.01	0.33±0.01	0.28±0.01	0.2418±0.0044	0.2109±0.0037
R^2	0,9977	0,9944	0,9946	0,9947	0,9948

Table A 4 – Values of equilibrium area per molecule, A_0, for each fixed surface area, π, ISOT18N.

Isotherm	ISOT18N		
π (mN m^{-1})	5.0	10.0	15.0
A_0 (nm^2 molecule^{-1})	0.230±0.005	0.180±0.004	0.152±0.004
R^2	0,9996	0,9997	0,9995

Table A 5 – Values of equilibrium area per molecule, A_0, for each fixed surface area, π, for ISOT18WE.

Isotherm	ISOT18WE		
π (mN m^{-1})	3.0	6.0	8.0
A_0 (nm^2 molecule^{-1})	0.21±0.01	0.17±0.01	0.15±0.01
R^2	0.9942	0.9943	0.9931

Note that error is infinite of A_0 value for the ISOTS1860, ISOTS18120, ISOT18N and ISOT18WE. This happened because the number of points used, for each pressure, was not enough to get a statistically relevant result.

Table A 6 – Values of equilibrium area per molecule, A_0, for each fixed surface area, π, for ISOTS1860.

Isotherm	ISOTS1860			
π (mN m^{-1})	20.0	25.0	30.0	40.0
A_0 (nm^2 molecule^{-1})	0,31±inf	0,27±inf	0,25±inf	0,19±inf
R^2	0,9830	0,9925	0,999996	0,9878

Table A 7 – Values of equilibrium area per molecule, A_0, for each fixed surface area, π, for ISOTS18120.

Isotherm	ISOTS18120		
π (mN m^{-1})	20.0	30.0	35.0
A_0 (nm^2 molecule^{-1})	0,29±inf	0,24±inf	0,21±inf
R^2	0,9894	0,9906	0,9902

Table A 8 – Values of equilibrium area per molecule, A_0, for each fixed surface area, π, for ISOTS18240.

Isotherm	ISOTS18240			
π (mN m^{-1})	20.0	25.0	30.0	40.0
A_0 (nm^2 molecule^{-1})	0.334±0.004	0.298±0.004	0.268±0.004	0.216±0.003
R^2	0.9986	0.9984	0.9983	0.9985

Table A 9 – Values of equilibrium area per molecule, A_0, for each fixed surface area, π, for ISOTS18N.

Isotherm	ISOTS18N			
π (mN m^{-1})	20.0	25.0	30.0	40.0
A_0 (nm^2 molecule^{-1})	0,30±inf	0,27±inf	0,24±inf	0,20±inf
R^2	0,99999995	0,9999	0,9979	0,9965

Table A 10 – Values of equilibrium area per molecule, A_0, for each fixed surface area, π, for ISOTS18WE.

Isotherm	ISOTS18WE			
π (mN m^{-1})	20.0	25.0	30.0	35.0
A_0 (nm^2 molecule^{-1})	0,23±inf	0,20±inf	0,17±inf	0,16±inf
R^2	0,9910	0,9909	0,9872	0,9987

Notes